LUT University

ASSESSING THE IMPACT OF VOLTAGE CONTROL VARIANTS IN SYNCHRONOUS GENERATORS ON INTERACTIONS WITH GRID-FORMING INVERTERS

Lappeenranta–Lahti University of Technology LUT

Degree Programme in Energy Technology, Master's thesis

2025

Ethan Graybrook-Paul

Examiners: Pasi Peltoniemi

Abstract

Lappeenranta–Lahti University of Technology LUT

LUT School of Energy Systems

Degree Programme in Energy Technology

In co-operation with Leibniz University Hannover

Ethan Graybrook-Paul

Assessing the Impact of Voltage Control Variants in Synchronous Generators on Interactions with Grid-Forming Inverters

Version 1.04/2025.08.13

Master's thesis

2025

67 pages, 35 figures, 7 tables and 1 appendix

Examiners: Pasi Peltoniemi

Keywords: Synchronous machine, grid forming inverters, excitation control, small-signal stability

The increasing capacity of renewable electricity generation has resulted in more grid-connected grid following inverters and fewer synchronous generators, which has been shown to erode network stability. Grid forming inverters are a potential solution as they can bolster network stability by emulating the grid supporting characteristics of synchronous machines, however their interactions with synchronous generators particularly at high penetration has been shown to be potentially destabilising for the grid.

This thesis explores the effect on excitation controls in these interactions, particularly how the controller type, be that proportional (P), proportional-integral (PI), or proportional-integral-derivative (PID), changes the small-signal stability of a coupled synchronous generator and grid forming inverter. An analytical model of a 1.4 GVA synchronous generator was derived and used to tune a PI and PID controller. The small-signal stability was then assessed via electromagnetic transient (EMT) simulations.

It was found that, while the system remained stable at nominal operating conditions, when system robustness was reduced the PI and PID controllers introduced instability phenomena which were not present in the P type controller. Introducing a power-system stabiliser (PSS) was found to be effective in mitigating instability. Additional factors related to the droop settings of the generator and inverter were tested and found to also impact stability.

General Symbol Conventions

Notation conventions

a	Variable
$\mathbf{a}$	Matrix
$\vec{a}$	Vector
$\underline{a}$	Complex number
$\bar{a}$	Per unit value
a^*	Reference value

Indices

0	Nominal
$\alpha\beta$	Value in the $\alpha\beta$-coordinate system
1d	d-axis damper winding
1q	First q-axis damper winding
2q	Second q-axis damper winding
abc	Value in the *abc*-coordinate system
d	d-axis component
dq	Value in the *dq*-coordinate system
e	Electrical
fd	Field winding
G	Grid (point of common coupling)
gen	Generator
inv	Inverter
m	Mechanical
q	q-axis component
T	Total

Symbol Definitions

$\mathbf{A}$	Plant matrix
$\mathbf{B}$	Control matrix
C	Capacitance
$\mathbf{C}$	Output matrix
$\mathbf{D}$	Feedforward matrix
E	Voltage
E_{A}	Internally induced voltage
E_{t}	Terminal voltage
f	Frequency
f_{LPF}	Inverter droop low-pass filter cut off frequency
G	Controller transfer function
H	Per unit inertia
i	Current
J	Inertia
K_{D}	Coefficient of damping torque
K_{D}	Controller derivative gain
K_{f}	Controller derivative filter gain
K_{I}	Controller integral gain
K_{P}	Controller proportional gain
K_{S}	Coefficient of synchronising torque
L	Inductance
L_{σ}	Leakage inductance
m_{p}	Inverter P-ω droop gain
p	Number of machine poles
P	Power
Q	Reactive power
R	Generator droop coefficient
S	Apparent power
s	Complex laplace variable
T	Time constant
t	Time
$\mathbf{T}_{\mathrm{C}}$	Clarke transformation matrix

$\mathbf{T}_\mathrm{P}$	Park transformation matrix
$\vec{u}$	State space input variables
X	Reactance
$\vec{x}$	State space state variables
X_d	Generator internal impedance
$\vec{y}$	State space output vector
Z	Impedance
Z_E	Line impedance
δ	Generator rotor angle
θ	Angular position of the generator rotor
v_l	Terminal voltage read by excitation system transducer
τ	Torque
τ_a	Accelerating torque
Φ	Flux
Ψ	Flux linkage
ω	Angular velocity
ω_LPF	Inverter droop low pass filter cut off angular frequency
ω_r	Rotor speed

Abbreviations

AC	Alternating Current
DC	Direct Current
EMT	Electromagnetic Transient
LPF	Low-pass filter
P	Proportional
PI	Proportional-integral
PID	Proportional-integral-derivative
PLL	Phase-locked loop
PSS	Power system stabiliser
VSM	Root mean square
RMS	Virtual synchronous machine

Declarations

Turnitin

The originality of this thesis has been reviewed with the Turnitin similarity checking service.

Ai usage

The author of the thesis, Ethan Graybrook-Paul, used the following AI-tools during the preparation of the thesis:

1. Github copilot (GPT-4.1)
    a. Assistance with LaTeX formatting
    b. Troubleshooting MATLAB code
2. DeepL
    a. Translation of non-English references

Responsibility

The author, Ethan Graybrook-Paul, takes full responsibility for the content of this thesis and has reviewed and edited the content generated by the possible use of AI tools.

Table of contents

Abstract

Symbols and abbreviations

Declarations

Table of contents 7

Lists of figures and tables (optional) 9

1 Introduction 11

2 Theoretical Background 13

2.1 Synchronous Generator 13

2.1.1 Operating Principle 14

2.1.2 Modelling 18

2.1.3 Excitation Systems 23

2.2 Power System Stability 26

2.2.1 Analysis of Small-Signal Instability 28

2.3 Grid Forming Inverters 30

2.4 PID Controllers 33

3 Simulation Models 35

3.1 Infinite Bus Model 35

3.1.1 Excitation Control Implementation 36

3.1.2 Frequency Control Implementation 38

3.2 Integrated Model 38

4 Analytical Model of the Synchronous Generator 42

4.1 Model Parameters 42

4.2 Analytical Model 42

4.2.1 Model Verification 48

4.3 Controller Tuning 49

4.3.1 PI Controller 50

4.3.2 PID Controller 51

4.3.3 Controller Verification 52
5 Assessment of Small-Signal Stability 54
5.1 Impact of Control Variants 54
5.2 Impact of Frequency Droop Cutoff Frequency 57
5.3 Impact of PSS 59
5.4 Impact of Frequency Droop Slopes 60
5.5 Identification of the Role of Inverter Droop Paths in Instability 60
6 Conclusion and Future Prospects 63
References 65
Appendices
Appendix 1 Analytical Model Coefficients
1.1 Calculation Coefficients 68
1.2 State space formula 69
1.2.1 Plant Matrix 69
1.2.2 Input Matrix 69

List of Figures

1 Schematic of a three-phase synchronous machine with an externally excited rotor (Kundur, 2009)
2 Structure of frequency control in a synchronous generator (Kundur, 2009)
3 Control block diagrams of a) Isochronous frequency control and b) droop frequency control (Kundur, 2009)
4 Sharing of load between two generators with different droop characteristics (Kundur, 2009)
5 Effect of load reference changes on the droop characteristic (Kundur, 2009)
6 Rotor and stator circuits in the physical three-phase reference frame (Kundur, 2009)
7 Equivalent circuits for a synchronous generator in the a) d-axis and b) q-axis (Kundur, 2009)
8 Basic excitation system control block diagram (Kundur, 2009)
9 V-Curve of a synchronous generator
10 Oscillation about a nominal operating point as shown in the power angle relation (Gibbard, Pourbeik & Vowles, 2015)
11 System instability via a) aperiodic drift with no excitation control and b) oscillation with excitation control (Kundur, 2009)
12 State space representation as a block diagram in the Laplace domain (Kundur, 2009)
13 Circuit approximation of a) grid following and b) grid forming converters (Rathnayake et al., 2021)
14 Block diagram of the a) parallel and b) standard implementation of a PID controller
15 PLECS schematic of the infinite bus model topology
16 Generator excitation system as modelled in PLECS
17 Implementation of the PID controller in PLECS
18 Frequency control implementation in PLECS
19 Single line diagram of the integrated model
20 Droop control paths of the grid forming inverter (Strunk & Mertens, 2023)
21 Grid forming inverter integration into synchronous generator model
22 A full simulation of the integrated model with a 100 km line length, $S = 1.3$ pu and 10% power step
23 Generator connected to an infinite bus
24 Synchronous machine as a voltage source behind an impedance connected to an infinite bus.

25 Field winding circuit for the a) d-axis and b) q-axis (Kundur, 2009)
26 Step response of the infinite bus analytical model H_2 and simulated model with a P controller
27 Bode plot of 7^{th}-order system transfer function and its 2^{nd}-order approximation
28 Comparison of P, PI and PID controller step response in an infinite bus and the excitation output
29 Step response of P, PI, and PID excitation controllers for 40 km line length, $f_{\text{LPF}} = 3$ Hz at $S = 1.3$ pu
30 Behaviour of PID and PI controlled excitation systems for a 40 km line length with $f_{\text{LPF}} = 3$ Hz at $S = 1.3$ pu
31 A sweep of f_{LPF} for a PI controller with 40km line length at $S = 1$ pu
32 A PID controlled excitation system with a 40 km line length at $S = 1.3$ pu with and without a PSS
33 Effect of droop slope setting on the rotor angle stability for a 40 km line length with $f_{\text{LPF}} = 3$ Hz at $S = 1$ pu
34 Power response of system with inverter droop paths disabled at $S = 1.3$ pu with $f_{\text{LPF}} = 3$ Hz and a 40 km line length
35 Output of inverter droop gains at $S = 1.3$ pu with $f_{\text{LPF}} = 3$ Hz and a 40 km line length

List of Tables

1 Physical parameters of infinite bus model
2 Physical parameters of the integrated model
3 Generator and inverter control parameters
4 The critical line length for each controller type. $S = 1.3$ pu, $f_{\text{LPF}} = 2$ Hz.
5 System stability with a PID controlled excitation system for a range of line lengths and f_{LPF}
6 System stability with a PI controlled excitation system for a range of line lengths and f_{LPF}
7 System stability with a P controlled excitation system for a range of line lengths and f_{LPF}

1 Introduction

Due to the increasing pressure of climate change, the composition of the electricity grid is rapidly shifting towards higher penetration of renewable resource based generation. Currently, the two leading resources by generation capacity are wind and solar, whose capacity increased by 326% in Europe between 2010 and 2023 (Eurostat, 2025).

These and other renewable resources require solid state power electronic based inverters to supply AC energy to the grid. Traditionally, inverters use a *grid following* control topology, which relies on measuring the grid voltage waveform with a phase-locked loop (PLL) and injecting current to supply power. The reliance on an existing voltage waveform means that grid following inverters alone cannot construct their own grid. This role has traditionally been performed by synchronous generators, which also provide other grid supporting characteristics that help maintain a stable grid. One such characteristic is inertia, which is provided by the combined rotating mass of the generators rotor and turbine. When a change in operating conditions occur, the rotating mass can either supply or absorb power in the form of kinetic energy, smoothing frequency deviations and promoting system stability (Tielens & Van Hertem, 2016). Grid following inverters do not provide these characteristics. It has been demonstrated that as the penetration of grid following inverters increases, grid stability is weakened (Markovic et al., 2021) (Zhang et al., 2023). If more electricity is to be supplied by renewable energy, new ways to bolster grid stability must be found.

Grid forming inverters, an emerging technology originating in microgrid applications, have been proposed as a potential solution to this problem. Instead of using a PLL, grid forming inverters use a modified control structure which emulates the characteristics of a synchronous generator, allowing them to construct their own voltage waveform and provide an emulated inertial response. Employing grid forming inverters alongside grid following inverters has been shown to improve both voltage and frequency stability (Zhang et al., 2023). However, in mixed grid situations involving synchronous generators, some studies have shown potentially destabilising interactions between the fast controls of a grid forming inverter and the slow controls of synchronous machines (Tayyebi et al., 2020), particularly as higher penetrations are reached.

The excitation system of the synchronous generator has been highlighted as a potential root of this instability (Markovic et al., 2021) (Crivellaro et al., 2020). However, these studies use simplified control models of the excitation system, particularly for the controller, which is often simplified to a single proportional gain. In reality, excitation systems are sophisticated and complex, employing a variety of structures and control types depending on the application (IEEE, 2016). Their effect on generator small-signal stability is also demonstrated

(Demello & Concordia, 1969), as they directly influence the machine's synchronising and damping torques, which are pivotal in designing robust systems. Thus, there is a gap in understanding around how more complex excitation systems interact with grid forming inverters and their effect on stability.

A generator's excitation systems is often coupled with a power system stabiliser (PSS), which is an auxiliary control system that augments the excitation control with the goal of reducing low frequency oscillations. The role of PSSs in stability interactions with grid forming inverters has been investigated (Markovic et al., 2021) (Crivellaro et al., 2020), but results are not consistent, and the role of tuning is highlighted as a crucial factor in whether its inclusion bolsters or erodes system robustness.

The goal of this thesis is to investigate the impact of excitation system control variants on the small-signal stability in interactions with grid forming inverters using Electromagnetic Transient (EMT) simulations. To this end, a model of a 1.4 GVA statically excited synchronous generator will be developed in PLECS. The excitation system will employ a PSS and three controller variants of P, PI and PID structures, which will be tuned to the generator using analytical methods and a derived analytical model of the generator. The generator will be coupled to a grid forming inverter model with a shared passive load. The small-signal stability of each variant will be assessed by subjecting the system to a small step load and observing the effect. The impact of other parameters which are known to affect stability, such as the virtual inverter inertia and droop gains, will also be tested.

2 Theoretical Background

This chapter will introduce the fundamental concepts used throughout this Master's thesis. It will cover the relevant theory of synchronous machines, including the parameterisation and control of applicable systems; fundamentals of power system stability and its analysis; the theory and structure of grid forming inverters, and their inertial properties; and finally an overview of PID controllers.

2.1 Synchronous Generator

Synchronous generators are electrical machines which are characterised by their ability to operate in synchronism with an external grid frequency. A synchronous machine consists of a stator and a rotor coupled together by a rotating magnetic field. The stator is made of a laminated core with equally spaced slots which host windings of current-carrying wire. These machines may act as either motors or generators.

There are many different types of synchronous generators with varying constructions. A synchronous generator may be connected to a 1-, 2-, or 3-phase system. The magnetic field produced by the rotor may come from embedded permanent magnets, or via an external excitation. The rotor shape may vary to leverage the so called 'reluctance effect' to create additional torque. For power generation applications, and for the purpose of this thesis, the typical construction is a 3-phase synchronous machine with an externally excited round rotor. This external excitation allows for the independent control of output voltage and the round rotor is more suited to rotation speeds associated with an electrical frequency of 50 Hz in thermal plants (Kundur, 2009), making this construction and optimal choice for power generation systems. Figure 1 depicts the cross-section of a stator and rotor within a synchronous generator.

In an externally excited synchronous machine, a direct current (DC) is fed to a set of windings in the rotor, known as field windings. These windings act as an electromagnet, producing a magnetic field with a strength proportional to the applied voltage. The rotor is driven by a prime mover, typically a thermal turbine, causing the rotor and its magnetic field to rotate. The rotating magnetic field causes a varying magnetic flux in the stator windings which, by Faraday's law of induction, results in an induced voltage. The frequency of the induced voltage is determined by the speed of its rotation and by the number of magnetic poles present in the machine. The relationship between these parameters is given by the formula

$$f = \frac{\omega_{\mathrm{r}}}{2\pi}\frac{p}{2} \tag{1}$$

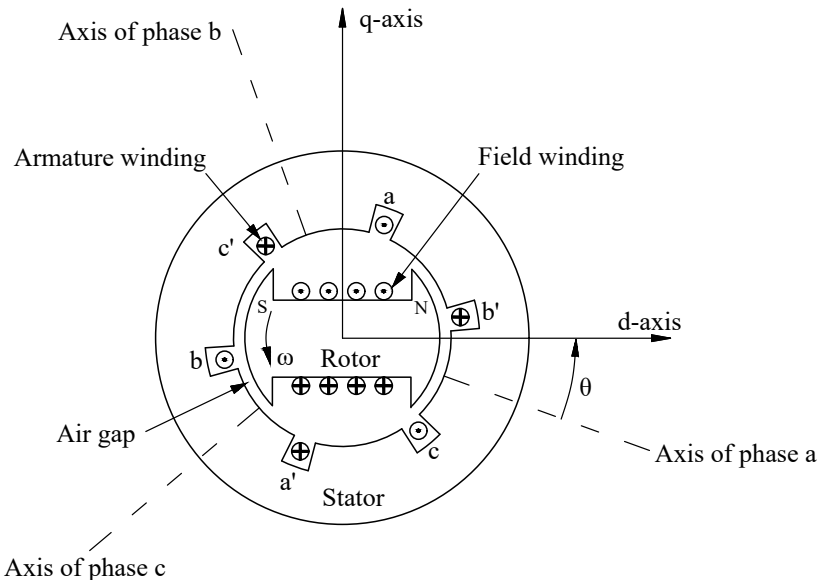

Figure 1: Schematic of a three-phase synchronous machine with an externally excited rotor (Kundur, 2009)

where f is the electrical frequency in the stator windings in Hz, ω_r is the rotational speed of the rotor in radians per second and p is the number of poles. The stator also produces its own magnetic field as a result of the connection with the external 50 Hz network. Unlike induction machines, which operate with the rotor and stator fields rotating at different speeds, synchronous machines have the speed of stator and rotor fields locked in synchronism, meaning that the rotor and stator frequencies remain equal during steady state operation.

Synchronous generators will also often include additional field windings known as damper windings (or amortisseur windings) which serve a stabilising function. Damper windings have constructions similar to that of a squirrel cage rotor (Pyrhönen, Jokinen & Hrabovcová, 2014), in that they consist of short-circuited conduction paths which are embedded in the rotor slots with the field winding. Many different damping coil constructions exist and their application varies among different machine constructions. In situations where the rotor speed changes suddenly, such as a transient disturbance, damping coils provide a counter field in response and thus smooth out disturbance effects and increase stability (Pyrhönen, Jokinen & Hrabovcová, 2014). They also aid in suppressing harmonics, particularly in unevenly loaded circuits, as well as increasing the effective synchronising torque of the machine (Damper Windings and Damping 2010).

2.1.1 Operating Principle

With the generator prime mover being driven at synchronous speeds, under no-load conditions the magnetic fields of the rotor and the stator are in alignment and no torque is produced. As an electrical load is introduced, the magnetic field of the stator will lag behind the

rotor's, producing a torque which acts against the rotation of the rotor. The angle between the two magnetic fields is known as the *rotor angle* δ (alternatively load angle or power angle) and is defined in the rotor's frame of reference. The rotor angle is a crucial parameter in synchronous machine operation, as it directly influences the machine's output power and stability, the former of which is defined as

$$P_{\mathrm{e}} = \frac{E_{\mathrm{t}} E_{\mathrm{A}}}{X_{\mathrm{d}}} \sin(\delta), \tag{2}$$

where E_{T} is the terminal voltage, E_{A} is the internally induced voltage in the stator and X_{d} is the machine reactance which inductive. It can be observed that as the rotor angle δ increases so does the power output until the critical angle $\delta = 90^{\circ}$, at which point the machine loses stability to the grid. The same equation can be used to describe the transfer of power across transmission lines by substituting the voltages of the sending and receiving points, and the rotor angle δ by the angle between the voltage phasors.

In an electrical network, the balance of active power and network frequency are directly coupled (Kundur, 2009). When the load power within the network increases it is experienced by the connected generators as an opposing torque on the shaft of the generator's prime mover. In order to provide more power, the generator must produce more torque to compensate, but the inherent inertia of the machine means that there is a delay between the load increasing and extra torque being provided, resulting in a decrease in speed and frequency. Similarly, when the load in a system decreases, the opposing torque on the generator shaft also decreases, resulting in an increase in frequency while the power to the prime mover is decreased. Hence, in an electrical network with an excess in generation, the frequency will be above the target frequency, and with an excess in load, the frequency will be less than the target. The goal of a frequency control system is to maintain the rotational speed of the shaft to a set target frequency. By increasing or decreasing torque to match load conditions, the active power of the generator is also controlled.

When a change in load condition occurs, there is an associated accelerating torque τ_{a} given by

$$\tau_{\mathrm{a}} = \tau_{\mathrm{m}} - \tau_{\mathrm{e}} \tag{3}$$

where τ_{m} is the mechanical torque and τ_{e} is the electrical torque in $\mathrm{N} \cdot \mathrm{m}$. This accelerating torque is applied on the shaft, which have an associated inertia J in $\mathrm{kg} \cdot \mathrm{m}^2$, expressed as

$$J \frac{d\omega_{\mathrm{r}}}{dt} = \tau_{\mathrm{a}} = \tau_{\mathrm{m}} - \tau_{\mathrm{e}}, \tag{4}$$

where ω_{r} is the angular velocity of the motor in rad/s. It is useful to express this equation in

terms of per-unit quantities, we define $\bar{H}$ as the per-unit inertial constant such that

$$\bar{H} = \frac{1}{2}\frac{J\omega_{0\mathrm{r}}^2}{S_{\mathrm{base}}}, \tag{5}$$

where $\omega_{0\mathrm{r}}$ is the rated mechanical rotation speed, equal to the rated electrical rotation speed divided by the number of poles. The torque and angular frequency can further be expressed as per-unit quantities, noting that $\tau_{\mathrm{base}} = S_{\mathrm{base}}/\omega_{0\mathrm{r}}$ and denoting per-unit quantities with a bar, this equation becomes

$$2\bar{H}\frac{d\bar{\omega}_{\mathrm{r}}}{dt} = \bar{\tau}_{\mathrm{m}} - \bar{\tau}_{\mathrm{e}}. \tag{6}$$

If Equation 6 is defined in terms of the angular position of the rotor θ in electrical radians, and an additional dampening torque is introduced which is proportional to the speed deviation and a dampening coefficient K_{D} then the resulting equation is what is commonly referred to as the *swing equation*, which describes the changes in rotor angle due to disturbances. This equation is crucial for the analysis of machine dynamics and is given by

$$\frac{2\bar{H}}{\omega_0}\frac{d^2\theta}{dt^2} = \bar{\tau}_{\mathrm{m}} - \bar{\tau}_{\mathrm{e}} - K_{\mathrm{D}}\Delta\bar{\omega}_{\mathrm{r}}. \tag{7}$$

Frequency Control

The power provided by the prime mover is determined by a *governor*, which controls a throttle altering the amount of working fluid, be that steam or gas, that is fed to the turbine. This is illustrated in Figure 2.

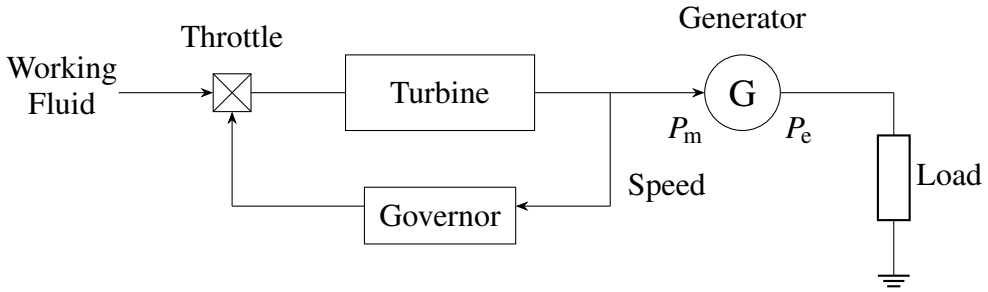

Figure 2: Structure of frequency control in a synchronous generator (Kundur, 2009)

The control logic applied in the governor determines the behaviour of the frequency and active power of the generator. Different control schemes are used depending on the requirements of the generator and of the network. An example of a simple frequency regulation scheme would be an *isochronous governor*, represented in Figure 3 a), which keeps the speed constant by controlling the governor proportionally to the error in speed. While this scheme would function effectively for a single generator, it would not be effective when many gen-

erators are connected to a single network, as it does not allow for an unequal share of power, or for different generators to have different nominal power setpoints, as the different control actions would be in constant conflict (Kundur, 2009).

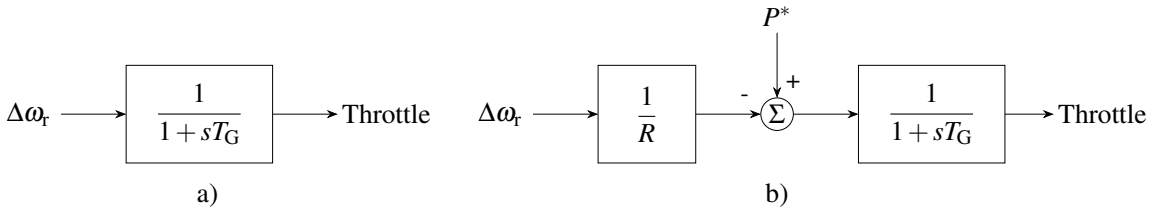

Figure 3: Control block diagrams of a) Isochronous frequency control and b) droop frequency control (Kundur, 2009)

Instead, *droop control* is commonly used which adds an inline gain of $1/R$, which determines the load characteristic. This is represented in Figure 3 b). This droop percentage R describes the relative change in power output per percentage in frequency deviation. For example, given a droop percentage of $R = 5\%$, if the frequency were to deviate 2.5% the power output would change by 50%. R is expressed as

$$R = \frac{\Delta f / f_0}{\Delta P / P_0} \cdot 100\% \tag{8}$$

where $\Delta f / f_0$ represents a percentage deviation from nominal frequency and $\Delta P / P_0$ represents a percentage deviation from nominal active power.

Different generators will have different droop characteristics depending on their allocated share of network load. For example, a generator with a smaller droop percentage would respond to an increase in demand (and an associated droop in system frequency) by increasing its power output by more than another generator with a larger droop percentage. Additionally, once the drooped power setpoints have been reached, the system will settle on a new different frequency f_1', shown in Figure 4, such that

$$\Delta f = f_1 - f_1' = \frac{\Delta P_1}{R_1} = \frac{\Delta P_2}{R_2}. \tag{9}$$

As shown in Figure 3 b) the droop control scheme also accepts a load reference P^* which is used as a power setpoint input. This effectively offsets the droop curve, allowing the generator power output to change while maintaining a constant frequency, as per Figure 5.

In real power systems, frequency control systems include additional components which maintain secondary objectives within the network. An example of which is maintaining the integral of the frequency, which ensures that timing functions associated with the grid

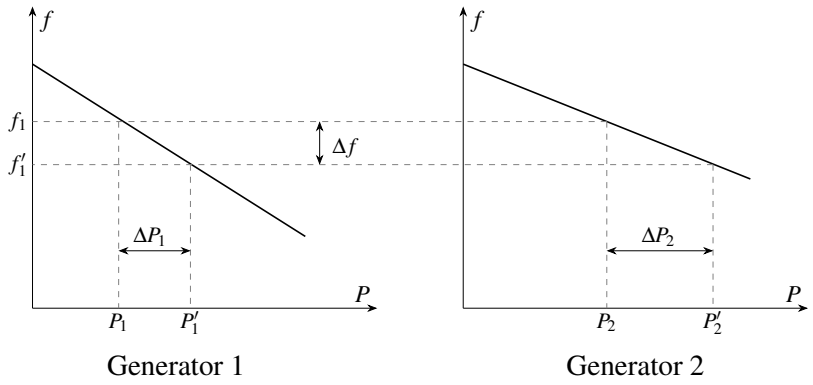

Figure 4: Sharing of load between two generators with different droop characteristics (Kundur, 2009)

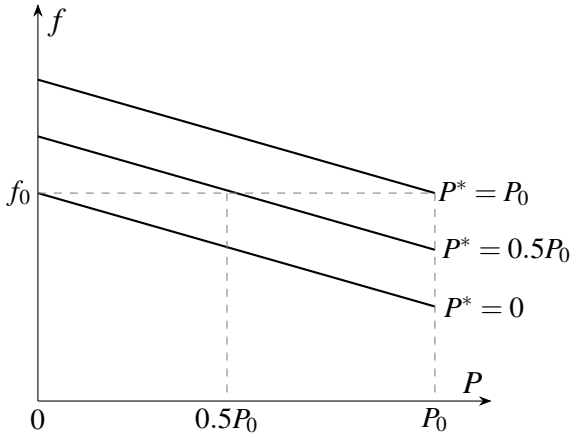

Figure 5: Effect of load reference changes on the droop characteristic (Kundur, 2009)

frequency, such as frequency based clocks, do not drift over time. However, for the purpose of this thesis, only droop control will be considered.

2.1.2 Modelling

Per-unit system

For the analysis of electrical quantities it is useful to define a per-unit system which normalises values around a standardised set of base quantities. A typical choice for synchronous generators is to define the per-unit system by the name plate ratings for the machine, normally given as apparent power S in VA, RMS line-to-line terminal voltage E in volts, and the electrical frequency f in Hz. All other quantities can be calculated from these base units, by

$$i_{\text{base}} = \frac{S_{\text{base}}}{\sqrt{3}E_{\text{base}}},\ \text{A} \qquad Z_{\text{base}} = \frac{E_{\text{base}}^2}{S_{\text{base}}},\ \Omega \qquad \omega_{\text{base}} = 2\pi f_{\text{base}},\ \text{elec. rad/s}$$
$$L_{\text{base}} = \frac{Z_{\text{base}}}{\omega_{\text{base}}},\ \text{H} \qquad \Psi_{\text{base}} = L_{\text{base}} i_{\text{base}},\ \text{V}\cdot\text{s} \qquad \tau_{\text{base}} = \frac{S_{\text{base}}}{\omega_{\text{base}}},\ \text{N}\cdot\text{m}.$$

The base quantities for the generator used in this thesis are defined in Table 1. A distinct per-unit system is defined for the excitation as described in Section 2.1.3

d-q transformation

It is convenient to a rotating reference frame to create time invariant machine relations. The d-q reference frame achieves this by defining a d-axis from the centre of the machine pointing towards the magnetic north of the rotor and a q-axis as being magnetically perpendicular to the d-axis, leading in the direction of rotation, as illustrated in Figure 1. We can convert stator quantities to this rotating reference frame by the way of the *Clarke* and *Park* transforms. The Clarke-transformation converts a column vector of quantities, for example voltages in the *abc* reference frame $\vec{e}_{\text{abc}}$, into the $\alpha\beta$ reference $\vec{e}_{\alpha\beta}$, which defines two stationary perpendicular axes with respect to the stators frame of reference. The transformation is performed with matrix $\mathbf{T}_{\text{C}}$ such that $\mathbf{T}_{\text{C}} \cdot \vec{e}_{\text{abc}} = \vec{e}_{\alpha\beta}$ with $\mathbf{T}_{\text{C}}$, in its power invariant form, defined as

$$\mathbf{T}_{\text{C}} = \sqrt{\frac{2}{3}} \begin{bmatrix} 1 & -\frac{1}{2} & -\frac{1}{2} \\ 0 & \frac{\sqrt{3}}{2} & -\frac{\sqrt{3}}{2} \\ \frac{1}{\sqrt{2}} & \frac{1}{\sqrt{2}} & \frac{1}{\sqrt{2}} \end{bmatrix}. \tag{10}$$

The Park-transformation builds upon the Clarke-transformation by adding a rotation to the reference axes, which are chosen to be attached to the rotation of the rotor with position θ. The transformation $\mathbf{T}_{\text{P}}$ such that $\mathbf{T}_{\text{P}} \cdot \vec{e}_{\text{abc}} = \vec{e}_{\text{dq}}$ is defined as

$$\mathbf{T}_{\text{P}} = \sqrt{\frac{2}{3}} \begin{bmatrix} \cos(\theta) & \cos\left(\theta - \frac{2\pi}{3}\right) & \cos\left(\theta + \frac{2\pi}{3}\right) \\ -\sin(\theta) & -\sin\left(\theta - \frac{2\pi}{3}\right) & -\sin\left(\theta + \frac{2\pi}{3}\right) \\ \frac{\sqrt{2}}{2} & \frac{\sqrt{2}}{2} & \frac{\sqrt{2}}{2} \end{bmatrix}. \tag{11}$$

In using the Park-transform, stator quantities and rotor quantities can be compared without any rotational components as a linear time-invariant system, significantly simplifying analysis.

Equivalent circuit model

In the electrical model of the synchronous generator, and generally in this thesis, the machine is assumed to be unaffected by magnetic saturation. While in a broad analysis of generator behaviour this is not a reasonable assumption to make, in this context, looking specifically at the small-signal stability, it is assumed that small-signal disturbances should not push the generator's operating conditions outside the non-saturated region, and therefore it need not be accounted for within the model. It is also assumed that the stator slots are 100% filled and that magnetic hysteresis is negligible.

An electrical model of a synchronous generator considers the separate rotor and stator circuits as well as their interaction via electromagnetic induction. The rotor circuit consists of a main d-axis field winding impedance $\underline{Z}_{\mathrm{fd}} = R_{\mathrm{fd}} + j\omega L_{\mathrm{fd}}$ along with the impedances of the damper coils, which can be resolved into two currents that flow in the d- and q- axis for the purpose of analysis $\underline{Z}_{1\mathrm{d}}$, $\underline{Z}_{1\mathrm{q}}$, and $\underline{Z}_{2\mathrm{q}}$. The stator circuit consists of impedances $\underline{Z}_{\mathrm{a}}$, $\underline{Z}_{\mathrm{b}}$, and $\underline{Z}_{\mathrm{c}}$ along each phase. These circuits are represented in Figure 6.

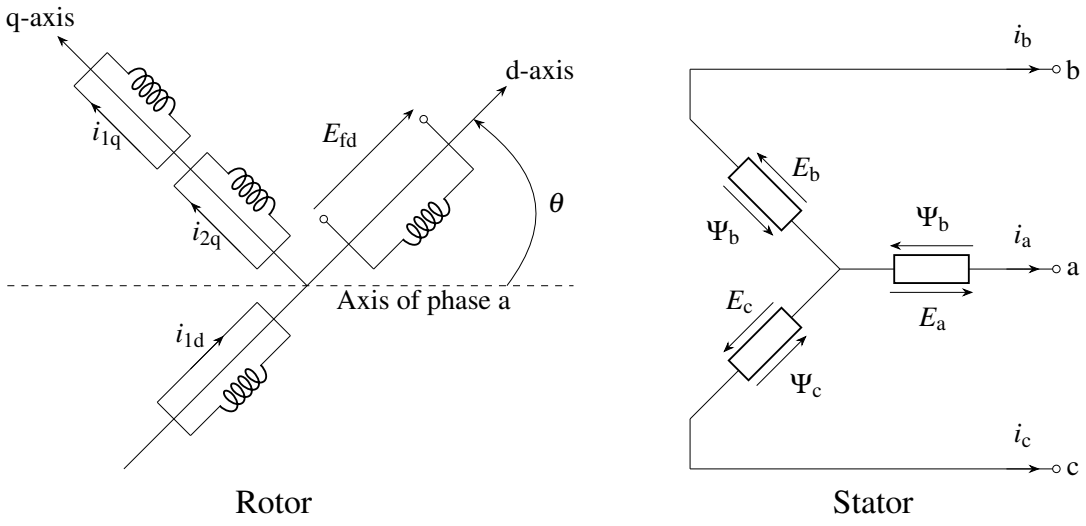

Figure 6: Rotor and stator circuits in the physical three-phase reference frame (Kundur, 2009)

The flux linkage Ψ of any inductor describes the relationship between the voltage and the magnetic flux in interaction with the coil. Each inductor in the rotor and stator influences both its own flux linkage, via its self inductance, and influences the other coils in the circuits, via their mutual inductances. There is also a portion of magnetic flux that does not couple with any coil, known as leakage inductance L_σ. In the *abc* reference, the mutual inductances between the coils will depend on the position of the rotor (except for mutual inductances between the rotor coils), and thus when the machine is in operation, they will change constantly with its rotation. This makes computation difficult, but is resolved by employing the

d-q transform.

The expression for flux linkage in phase-a of the stator is given by

$$\begin{aligned}\Psi_{\mathrm{a}} = & -i_{\mathrm{a}}\left[L_{\mathrm{aa0}}+L_{\mathrm{aa2}}\cos(2\theta)\right]+i_{\mathrm{b}}\left[L_{\mathrm{ab0}}+L_{\mathrm{aa2}}\cos\left(2\theta+\frac{\pi}{3}\right)\right] \\ & +i_{\mathrm{c}}\left[L_{\mathrm{ab0}}+L_{\mathrm{aa2}}\cos\left(2\theta-\frac{\pi}{3}\right)\right]+i_{\mathrm{fd}}L_{\mathrm{afd}}\cos(\theta) \\ & +i_{\mathrm{1d}}L_{\mathrm{a1d}}\cos(\theta)-i_{\mathrm{1q}}L_{\mathrm{a1q}}\sin(\theta)-i_{\mathrm{2q}}L_{\mathrm{a2q}}\sin(\theta),\end{aligned} \tag{12}$$

Expressions in a similar form can be obtained for phase-b and phase-c of the generator. By applying the d-q transform to the flux linkages and currents, we can obtain an expression for an equivalent d- and q- axis flux linkage in the stator by

$$\begin{aligned}\Psi_{\mathrm{d}} &= -(L_{\mathrm{aa0}}+L_{\mathrm{ab0}}+\frac{3}{2}L_{\mathrm{aa2}})i_{\mathrm{d}}+L_{\mathrm{afd}}i_{\mathrm{fd}}+L_{\mathrm{a1d}}i_{\mathrm{1d}} \\ \Psi_{\mathrm{q}} &= -(L_{\mathrm{aa0}}+L_{\mathrm{ab0}}-\frac{3}{2}L_{\mathrm{aa2}})i_{\mathrm{q}}+L_{\mathrm{a1q}}i_{\mathrm{1q}}+L_{\mathrm{a2q}}i_{\mathrm{2q}} \\ \Psi_{0} &= -(L_{\mathrm{aa0}}-2L_{\mathrm{ab0}})i_{0},\end{aligned} \tag{13}$$

where L_{ab0}, L_{afd}, L_{a1d}, L_{a1q}, and L_{a2q} are mutual inductances, and L_{aa0} is the a-phase self inductance. Since the inductance varies sinusoidally with the rotation of the rotor in the *abc* frame, inductances denoted with L_0 represent the mean inductance, and L_2 represent the maximum deviation from the mean.

From these relations we can define new d- and q- axis inductances by

$$\begin{aligned}L_{\mathrm{d}} &= L_{\mathrm{aa0}}+L_{\mathrm{ab0}}+\frac{3}{2}L_{\mathrm{aa2}} \\ L_{\mathrm{q}} &= L_{\mathrm{aa0}}+L_{\mathrm{ab0}}-\frac{3}{2}L_{\mathrm{aa2}} \\ L_{0} &= L_{\mathrm{aa0}}-2L_{\mathrm{ab0}}.\end{aligned} \tag{14}$$

The relationships between the inductances can be further simplified by adding upon the per-unit system and defining an additional base for the rotor. Denoting per-unit inductances as $\bar{L}$, we may introduce a new base with two goals: to make all mutual inductances reciprocal, i.e. $\bar{L}_{\mathrm{afd}} = \bar{L}_{\mathrm{fda}}$, and to make mutual inductances in each axis equal, i.e. $\bar{L}_{\mathrm{afd}} = \bar{L}_{\mathrm{a1d}}$. This is achieved by introducing the $\mathrm{L_{ad}}$-base reciprocal system, which defines a set of mutual inductances terms $\bar{L}_{\mathrm{ad}}$ and $\bar{L}_{\mathrm{aq}}$ which represent the d- and q- axis mutual inductances in the

stator due to the rotor such that

$$\begin{aligned} \bar{L}_{\mathrm{d}} &= \bar{L}_{\sigma} + \bar{L}_{\mathrm{ad}} \\ \bar{L}_{\mathrm{q}} &= \bar{L}_{\sigma} + \bar{L}_{\mathrm{aq}}. \end{aligned} \tag{15}$$

In order to achieve the stated goals, a base current for each rotor circuit it defined such that

$$\begin{aligned} i_{\mathrm{fd,base}} &= \frac{\bar{L}_{\mathrm{ad}}}{\bar{L}_{\mathrm{afd}}} i_{\mathrm{base}} \quad i_{\mathrm{1d,base}} = \frac{\bar{L}_{\mathrm{ad}}}{\bar{L}_{\mathrm{a1d}}} i_{\mathrm{base}} \\ i_{\mathrm{1q,base}} &= \frac{\bar{L}_{\mathrm{ad}}}{\bar{L}_{\mathrm{a1q}}} i_{\mathrm{base}} \quad i_{\mathrm{2q,base}} = \frac{\bar{L}_{\mathrm{ad}}}{\bar{L}_{\mathrm{a2q}}} i_{\mathrm{base}}. \end{aligned} \tag{16}$$

All quantities henceforth will be given as per-unit values and so the bar notation is disregarded. The complete equivalent circuits for a synchronous generator in the d-q reference frame can be formulated based on the voltage and current relations of the rotor and stator circuits. The equivalent circuits are shown in Figure 7.

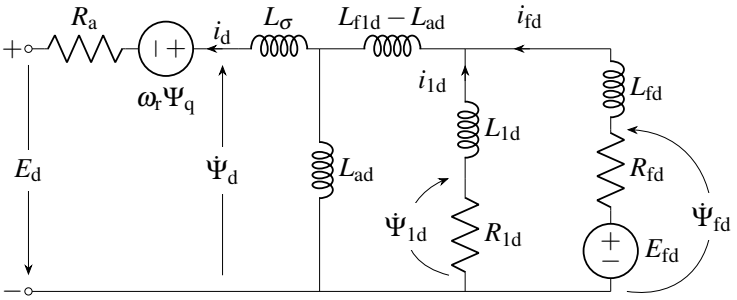

a)

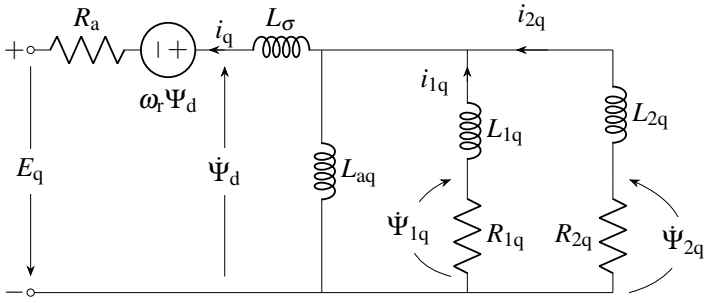

b)

Figure 7: Equivalent circuits for a synchronous generator in the a) d-axis and b) q-axis (Kundur, 2009)

2.1.3 Excitation Systems

In a synchronous machine, the internally generated voltage is proportional to the flux in the air gap Φ_A, in webers, and the speed of the rotor (Chapman, 2005)

$$E_A \propto \Phi_A \omega. \tag{17}$$

The flux in the machine is dependent on the current in the rotor field winding i_{fd} and its associated magnetization curve. The field winding current is controlled by a variable voltage source which is influenced by the measured terminal voltage E_t of the generator. An exciter provides the DC voltage to the field windings and a transducer measures the terminal voltage to provide the signal to the controller. The system also includes protective circuits which limit the output of the exciter and performs other protective functions. Optionally, a system may introduce a PSS which improves system stability by providing additional oscillation damping.

There are three configurations of exciters: AC exciters, DC exciters, and static exciters. *AC exciters* couple directly to the generator's shaft and use secondary alternators to produce an AC current. This current is then converted to the required DC current by the means of rectifiers. *DC exciters* use DC generators to generate excitation power which is then provided to the field windings via slip rings. The DC generator may be coupled to the shaft or driven by an external motor. While DC exciters were common in the past, they have since been replaced with AC exciters and static exciters (Boldea, 2006). *Static exciters* use a separate auxiliary power supply with solid state power converters and supply current to the field winding via slip rings or brushes. For the purpose of this thesis, the generator is assumed to use a static excitation system.

The basic control model of a static excitation system consists of a voltage transducer with an associated time constant T_R, a voltage reference signal E^*, and a controller with function $G(s)$. The control loop compares the measured terminal voltage E_t with the reference voltage and feeds the error signal to the controller, as represented in Figure 8.

The control of the excitation system also has a bearing on the power factor of the generator's output. A generator is said to be over- or underexcited depending on the relationship between the internally induced voltage E_A and the terminal voltage E_t. The relationship between the excitation current and the power factor is defined by the *V-Curve* as shown in Figure 9. In the underexcited condition the field excitation is relatively small, which causes the internally induced voltage to be lower than the terminal voltage and results in a lagging current phasor, associated with inductive loads. In the overexcited state, the field excitation is high, resulting in an internally induced voltage which is higher than the terminal voltage causing the current

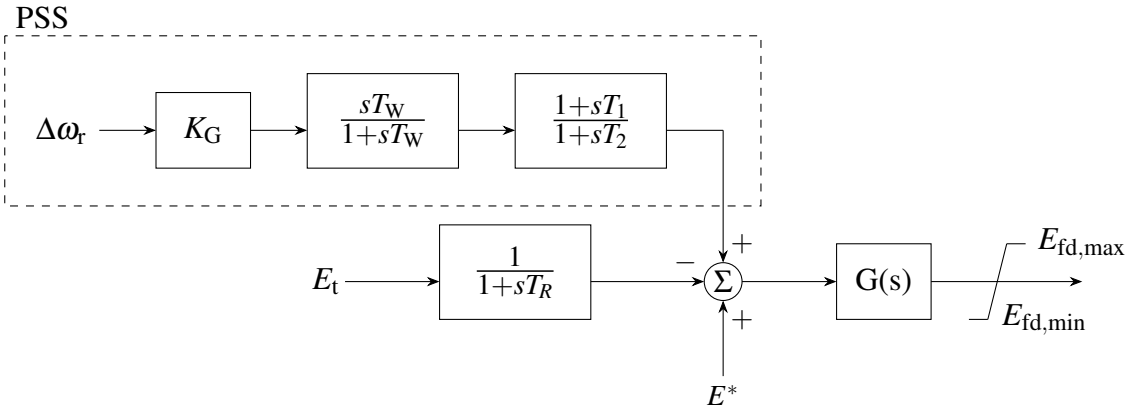

Figure 8: Basic excitation system control block diagram (Kundur, 2009)

phasor to lead the voltage, associated with capacitive loads. In this way, by controlling the excitation of the field windings the power factor of the generator can be adjusted.

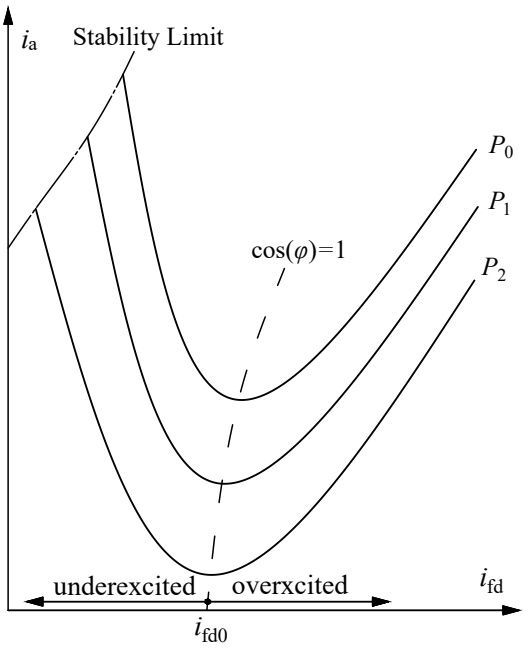

Figure 9: V-Curve of a synchronous generator

Excitation Per-unit system

Since the voltage and currents in the field windings are very small compared to the generator quantities, it is often convenient to introduce a separate per-unit system for use in the excitation system. There are several options, but a common approach is the *non-reciprocal* pu system which defines the nominal voltage of the field circuit $E_{fd,base}$ as that which produces a nominal terminal voltage at nominal speed. The voltage induced in the stator windings is proportional to the current in the field winding i_{fd} and the mutual inductance between the

rotor and the stator in the d-axis L_{ad}

$$E_{\text{t}} = L_{\text{ad}} i_{\text{fd}} = 1.0 \text{ pu}, \tag{18}$$

thus the per-unit field current is given by

$$i_{\text{fd,base}} = \frac{1}{L_{\text{ad}}}. \tag{19}$$

The corresponding field voltage is related to the field winding resistance R_{fd} by

$$E_{\text{fd,base}} = R_{\text{fd}}\, i_{\text{fd}} = \frac{R_{\text{fd}}}{L_{\text{adu}}} \tag{20}$$

This is not equivalent to the L_{ad}-base pu system introduced earlier, and so to compare quantities between the excitation system and the stator or rotor they must be converted across the two systems.

Power System Stabilisers

A PSS is an additional subsystem added to the excitation system which augments its control action with the goal of increasing stability. Specifically, its aim is to stabilise low frequency oscillations between 0.2 and 2.5 Hz (Gibbard, Pourbeik & Vowles, 2015) by influencing the components of the machine's torque which are in phase with speed variations, thus increasing the effective damping.

The excitation system can influence both the synchronising and damping torques of the generator (Kundur, 2009). While the effect on the synchronising torque is usually insignificant, the excitation system can influence the machine's damping torque very significantly, which acts in phase with the speed of the rotor and reduces the amplitude of oscillations over time. Ideally, the PSS would provide a direct feedback based on the variation in rotor speed $\Delta\omega$. However, for the damping to be effective the gain must be completely in phase with the speed variations, which is not possible using direct feedback due to the delay associated with the excitation system itself. As a result the PSS must be tuned to the excitation system so that its lag is compensated. This is done by means of a lag compensator which offsets the phase lag for a specific band of frequencies, chosen to be the $0.2 \ldots 2.5$ Hz range of frequency oscillations (Kundur, 2009). A lead compensator is also introduced which normalises the gain for higher frequency oscillations. A washout filter, with associated time constant T_{w}, is included which filters out much lower frequency signals, and finally a stabilising gain K_{G} influenced the magnitude of the damping force. The structure of a PSS is shown in Figure 8.

Alternative PSS structures can exist which take different signals as an input. ΔP type power

system stabilisers aim to improve stability by targeting power oscillations and increase excitation when power decreases. Δf type PSSs function similarly to the $\Delta\omega$ variant and decrease excitation when the frequency decreases (Li, 2019). $\Delta\omega$ type PSSs will be considered for this thesis.

2.2 Power System Stability

Power system stability describes the capability of an electrical power system to maintain equilibrium during standard conditions and to return to a functioning operating state following a disturbance. The analysis of power system stability is typically viewed through the lens of the synchronous machine, as the fundamental principles that govern stability are emergent from the interactions of these machines with the wider network.

There are two forces that allow a synchronous generator to maintain equilibrium with its connected network, the so called synchronising torque T_{S} and the damping torque T_{D}. Say a network is subjected to a disturbance, causing the effective reactance from the perspective of a generator to increase. Since the total reactance increases, the power output from the generator immediately falls from P_0 to P_1. However, the mechanical power from the prime mover P_{m} (which in the per-unit system is nominally equal to the torque) remains the same as the pre-disturbance power P_0, thus the rotor begins to accelerate, causing the angle between the rotor and the grid voltage phasors to increase from δ_1. From Equation 2 the power then starts to increase due to the growing power angle. The power will continue to increase until the electrical power equals the mechanical power at δ_0, at which point the torques are balanced and the acceleration on the rotor equals zero. However, due to the inertia of the rotor, the rotor angle will continue to increase, producing more power but being subject to a decelerating force due to the now greater electrical torque than mechanical torque. At the point δ_2 the decelerating force halts the increase in rotor angle and begins to decrease it, reducing power output. These operating points with respect to the power angle relation are shown in Figure 10.

The restoring torque that brings the rotor back to nominal is the *synchronising torque*. Under these conditions, the oscillation around the nominal operating point would continue indefinitely if not for the damping torque, which slows each oscillation until the system settles at nominal (Gibbard, Pourbeik & Vowles, 2015). In this way the damping torque is said to be in phase with the rotor speed ω and the synchronising torque in phase with the rotor angle, such that

$$\Delta\tau_{\mathrm{m}} = K_{\mathrm{S}}\Delta\delta + K_{\mathrm{D}}\Delta\omega. \tag{21}$$

The causes of instability phenomena are multifaceted and complex, therefore different types

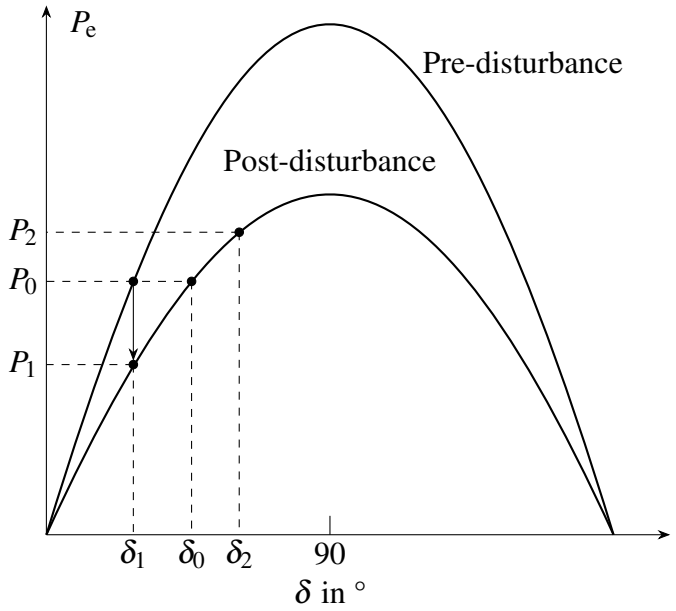

Figure 10: Oscillation about a nominal operating point as shown in the power angle relation (Gibbard, Pourbeik & Vowles, 2015)

of instability phenomena are split into classifications and their analysis and treatment are performed uniquely. So far, the type of stability discussed has been *rotor angle stability*, which describes the ability of a machine to maintain synchronism to the network while being subjected to a disturbance (Definition and Classification of Power System Stability IEEE/-CIGRE Joint Task Force on Stability Terms and Definitions 2004). This type of instability will be the main focus of this thesis. Voltage stability is another classification, which refers to a systems ability to maintain voltage at certain nodes, however this can be closely related to rotor stability (Gibbard, Pourbeik & Vowles, 2015). Finally, the third classification is frequency stability, which relates to the equilibrium of supply and demand capacity to maintain a nominal grid frequency, and thus has little to do with the control of machines.

Rotor angle stability can also be classified depending on the type of disturbance the system is subjected to. Large disturbances, such as the tripping of heavily loaded lines, relates to the *transient stability* of the system. Transient stability analysis is highly non-linear and, if stability is maintained, usually results in the system re-settling to a significantly different operating point than before the disturbance (Kundur, 2009). Contrastingly, small disturbances, such as the switching of small loads, concern the *small-signal stability* of the system. This classification is characterised by the ability to analyse the system using a set of linearised equations, reducing the computational complexity significantly. Of small-signal instability phenomena, two types can be further classified. Situations in which the rotor angle drifts away from the nominal operating point, known as aperiodic drift, are due to a lack of synchronising torque and occur in systems with a constant field voltage, that is to say, no exci-

tation control. Alternatively, instabilities which oscillate about the nominal operating point are known as oscillatory instability. They are due to insufficient damping torque and occur in voltage regulated systems (Kundur, 2009).The types of small-signal instabilities are illustrated in Figure 11.

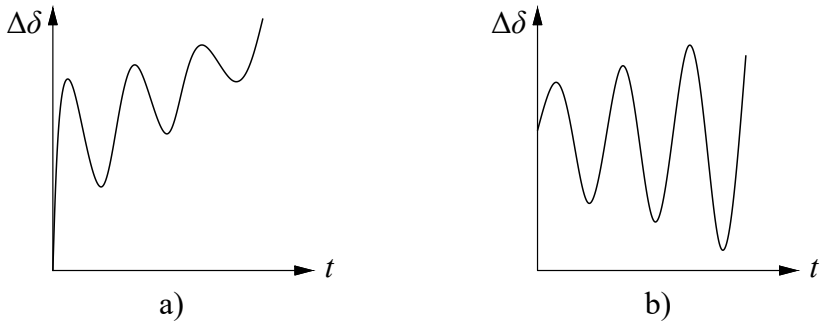

Figure 11: System instability via a) aperiodic drift with no excitation control and b) oscillation with excitation control (Kundur, 2009)

An excitation system is able to influence the stability of the generator due to its ability to shift the power-angle response by responding to disturbances and changing the internally generated voltage. When required, an excitation system could choose to change the internally generated voltage, which by Equation 2 can increase or decrease the electrical power and torque, thus influencing the magnitude of the restoring torque.

2.2.1 Analysis of Small-Signal Instability

Generally, dynamical systems, such as power systems, are modelled as a set of time dependent non-linear equations which govern the relationships between the different operating parameters. For the purpose of analysis, it is useful to know what the behaviour of the system would be for an arbitrary time t and for a set of initial conditions and inputs. Such a view of the system can be derived in *state space* using a set of state equations and variables. In this formulation, the state of the system can be represented by a vector $\vec{x}$ which contains a set of $n-$state variables, and subjected to a set of $m-$input variables in $\vec{u}$ such that

$$\vec{x} = \begin{bmatrix} x_1(t) \\ x_2(t) \\ \vdots \\ x_n(t) \end{bmatrix} \qquad \vec{u} = \begin{bmatrix} u_1(t) \\ u_2(t) \\ \vdots \\ u_m(t) \end{bmatrix}. \tag{22}$$

If the evolution of the system over time is itself time independent, the system is said to be *autonomous* and the evolution of the state variables can be represented as

$$\dot{\vec{x}} = \vec{f}(\vec{x}, \vec{u}). \tag{23}$$

We may also like to extract information about some output variables $\vec{y}$ which are not state variables. They may be expressed as

$$\vec{y} = \vec{g}(\vec{x}, \vec{u}). \tag{24}$$

So far, the functions $\vec{f}$ and $\vec{g}$ consist of a set of non-linear equations determined by the dynamics of the system, however non-linearity makes computation difficult and the vast array of linear control theory tools cannot be applied. Therefore, it is advantageous to linearise the state equations about an operating point. We define a new variable $\vec{\Delta x}$ which describes the perturbation about some initial operating point $\vec{x}_0$ such that

$$\vec{x} = \vec{\Delta x} + \vec{x}_0. \tag{25}$$

We know this is a valid approximation due to the Poincaré theorem on linear stability, which states that if a linearised system is stable about an operating point then the non-linear system is also stable at that point. Additionally, if the system is subject to a sufficiently small disturbance then the response of the linearised system is equal to that of the non-linear system (Gibbard, Pourbeik & Vowles, 2015). We choose the initial operating point as a stable one such that $\vec{\dot{x}}_0 = \vec{f}(\vec{x}_0, \vec{u}_0) = \vec{0}$. Given the definition in Equation 25, the perturbed system can be represented as

$$\begin{aligned} \vec{\dot{x}} &= \vec{\Delta \dot{x}} + \vec{\dot{x}}_0 \\ &= \vec{f}[(\vec{x}_0 + \vec{\Delta x}), (\vec{u}_0 + \vec{\Delta u})]. \end{aligned} \tag{26}$$

Given the disturbance is sufficiently small, the functions in $\vec{f}$ may be expressed as a first-order Taylor's series expansion, such that

$$\Delta \dot{x}_i = \frac{\partial f_i}{\partial x_1}\Delta x_1 + \cdots + \frac{\partial f_i}{\partial x_n}\Delta x_1 + \frac{\partial f_i}{\partial u_1}\Delta u_1 + \cdots + \frac{\partial f_i}{\partial u_m}\Delta u_m. \tag{27}$$

The expressions in the output function $\vec{g}$ can be expressed in the same way. The result are two linearised systems of equations in the form

$$\begin{aligned} \vec{\Delta \dot{x}} &= \mathbf{A}\vec{\Delta x} + \mathbf{B}\vec{\Delta u} \\ \vec{\Delta y} &= \mathbf{C}\vec{\Delta x} + \mathbf{D}\vec{\Delta u}, \end{aligned} \tag{28}$$

where $\mathbf{A}$ is the plant matrix populated with the partial derivatives $\partial f_i / \partial x_j$, $\mathbf{B}$ is the control matrix with $\partial f_i / \partial u_j$, $\mathbf{C}$ is the output matrix with $\partial g_i / \partial x_j$, and $\mathbf{D}$ is the feedforward matrix with $\partial g_i / \partial u_j$. The structure of the state space representation is shown in Figure 12.

The system of Equation 28 can be represented in the Laplace domain by performing the

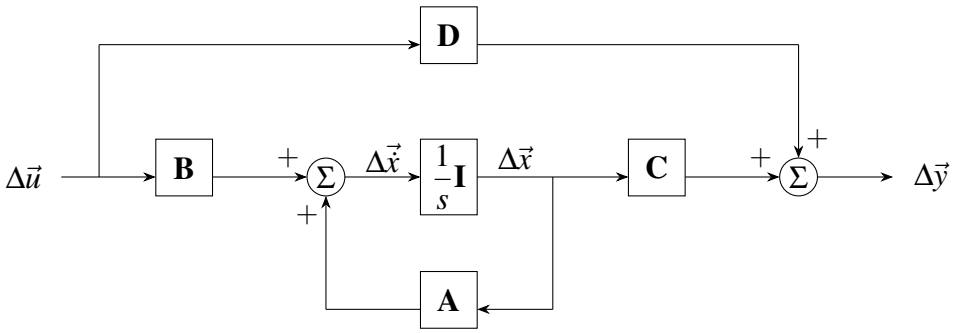

Figure 12: State space representation as a block diagram in the Laplace domain (Kundur, 2009)

Laplace transformation. The resulting state equations are

$$\begin{aligned} s\vec{\Delta}x(s) - \vec{\Delta}x(0) &= \mathbf{A}\vec{\Delta}x(s) + \mathbf{B}\vec{\Delta}u(s) \\ \Delta\vec{y}(s) &= \mathbf{C}\Delta\vec{x}(s) + \mathbf{D}\Delta\vec{u}(s). \end{aligned} \tag{29}$$

By rearranging these equations we can obtain solutions to the state and output perturbations by

$$\begin{aligned} \vec{\Delta}x(s) &= (s\mathbf{I} - \mathbf{A})^{-1}[\vec{\Delta}x(0) + \mathbf{B}\vec{\Delta}u(s)] \\ \vec{\Delta}y(s) &= \mathbf{C}(s\mathbf{I} - \mathbf{A})^{-1}[\vec{\Delta}x(0) + \mathbf{B}\vec{\Delta}u(s)] + \mathbf{D}\vec{\Delta}u(s) \end{aligned} \tag{30}$$

2.3 Grid Forming Inverters

Grid forming inverters are an emerging technology that aim to emulate the beneficial characteristics of traditional synchronous generators by using power electronic components and novel control methods. They are a development upon the traditional grid following inverters, which have seen a rapid increase in installation capacity in recent years. However, the rise of grid following inverters has highlighted fundamental issues regarding their ability to support the grid as their penetration increases, namely in providing smoothing for frequency deviations and fault response characteristics. Grid forming inverters aim to address these issues by modifying their control structures to re-introduce inertial and smoothing characteristics that are usually performed by synchronous generators.

A grid following inverter acts as an ideal current source in parallel with an impedance, as shown in Figure 13 a). The voltage at the point of common coupling (PCC) is measured to extract the voltage phasor, which describes the frequency and phase angle. This is calculated using a PLL. The grid following inverter synchronises to the voltage at the PCC and injects current according to active and reactive power setpoints P^* and Q^* respectively. Additional

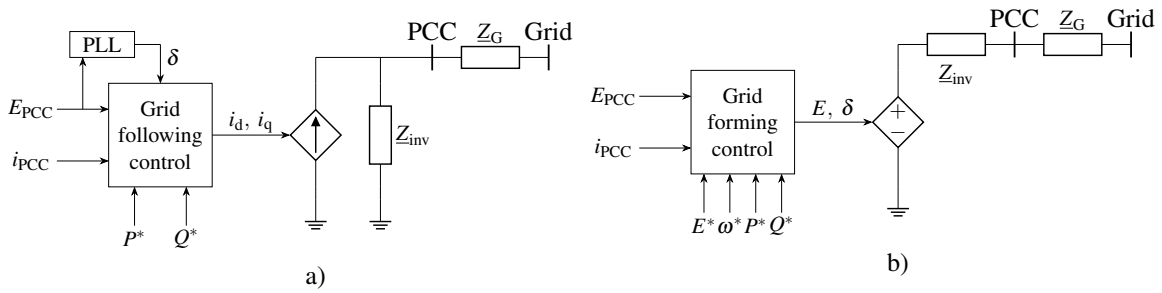

Figure 13: Circuit approximation of a) grid following and b) grid forming converters (Rathnayake et al., 2021)

control loops can be introduced to provide some grid support under this scheme, namely *droop control* which can support the grid frequency by changing the active power setpoint, or support the voltage by changing the reactive power setpoint. However, there are issues with this implementation. Firstly, grid following inverters cannot provide any voltage regulation, as their voltage is completely determined by the PCC voltage phasor. This is particularly problematic in weak-grid scenarios, as the measured voltage phasor may be subject to more frequent transient disturbances or deviations, resulting in suboptimal power injection which can reduce small-signal and transient stability (Rathnayake et al., 2021). Secondly, grid following inverters provide no inertial response to sudden changes in frequency. Where a synchronous machine can resist such a change due the inertia associated with the rotating mass of the rotor, a grid following inverter cannot, due to its locked dependence on the grid frequency. Low inertia power systems are characterised by a lack of damping to changes in frequency, this results in reduced system stability and an increased difficulty in maintaining a regulated grid frequency. Thus, for a healthy grid it is vital that connected generators provide a sufficient inertial response.

By contrast, grid forming inverters act as a voltage source with a small series impedance, as shown Figure 13 b). The inverter can generate a voltage waveform at a given frequency completely independently of the grid, allowing the inverter to operate either as an islanded system or with an independent phase angle. The main objective of the outer control loops is to regulate the voltage and frequency at the PCC which results in an indirect control of the active and reactive power injection, similar to the operation of a synchronous generator. This is enormously beneficial in supporting the grid for several reasons. Grid forming inverters are able to bolster weak grids by providing a consistent voltage waveform and damp grid disturbances. Additionally, by acting as a voltage source, the power transfer to the grid is described by the power-angle relation of Equation 2. In the event of a disturbance there is a rapid change in the grid phase angle, but since the grid forming inverter regulates its own phase angle the power transfer will increase instantaneously. This is beneficial for situations such as step load changes where rapid power delivery can reduce the transient response to

the disturbance (Sauer & Pai, 2007).

Another key advantage of grid forming inverters is their ability to provide an inertial response. This can be achieved through the modelling of synchronous machine dynamics within the control loop and an associated emulation of inertial characteristics. This is known as *virtual synchronous machine* (VSM) control (Rathnayake et al., 2021). The most simple form of this is the emulation of the swing equation, as stated in Equation 7, which models the change in rotor angle as a function of the changing electrical demand and the inertia of the rotor. An analogous implementation within a grid forming inverter might set the angular frequency of the inverter ω_e by (D'Arco & Suul, 2014)

$$T_\mathrm{b} \cdot s \cdot \omega_\mathrm{m} \approx P^* - P_\mathrm{e} - K_\mathrm{D}(\omega_\mathrm{e} - \omega_\mathrm{G}), \tag{31}$$

where ω_G is the grid angular frequency, P^* the reference power, P_e the inverter power output, and T_b the inertial time constant associated with the virtual synchronous machine. Also like synchronous generators, grid forming inverters may have a control loop to implement droop control so that multiple units may operate in parallel and share the load according to their droop constant m_p as defined in Section 2.1.1. It is common to include a low-pass filter as part of the droop control, with a corner frequency f_LPF in Hz, in order to filter out high-order harmonics or disturbances in the PCC measurement. However, it has been demonstrated in (D'Arco & Suul, 2014) that a droop-control implementation with a low-pass filter is mathematically equivalent to a virtual synchronous machine implementation, with the inertial response related by

$$T_\mathrm{b} = \frac{1}{f_\mathrm{LPF}\, m_\mathrm{p}} \qquad K_\mathrm{D} = \frac{1}{m_\mathrm{p}}. \tag{32}$$

So, as the corner frequency of the low pass filter is reduced, the higher the inertial time constant and thus inertia of the inverter. However, it has been shown that reducing the corner frequency introduces a phase-lag within the active power control loop which can reduce small-signal stability (Wu et al., 2016). Thus, choosing a suitable corner frequency is a trade-off between providing enough inertia without compromising the phase margin of the control.

Other small-signal stability characteristics of both classes of converters are emergent from their representation as either a voltage source or current source. Grid following inverters, as discussed, have poor small-signal stability in weak grid situations, due to their dependence on potentially unstable voltage references. However, while grid forming inverters have a strong small-signal stability in these weak grid scenarios, in strong grid scenarios their small-

signal stability is reduced. This is due to the interactions of ideal voltage sources with a small connecting line impedance, which can result in large transient currents and potentially induce instability (Strunk & Mertens, 2023).

2.4 PID Controllers

In dynamical systems, it is often a goal to control a single or a set of output values with respect to a single or a set of input values. Controllers which perform these functions are tailored to the characteristics of the system they are trying to control and may take on different structures in order to achieve the defined performance goals. One such structure is the PID controller, which is a popular controller, adopted by more than 50% of deployed field controllers (Ogata, 2022). PID stands for *proportional-integral-derivative* which are the three control actions forming the controller.

A PID controller is a closed loop device that accepts an error signal $e(t)$ and outputs a control signal $u(t)$ to the plant. The controller may be implemented in a standard form or in a parallel form, as shown in Figure 14. Both forms are equivalent and can be freely converted into the other form by transforming the gain coefficients K_P, K_D, and K_I which define the effect that each action has. A parallel controller, the structure considered by this thesis, will have the corresponding transfer function

$$\frac{u(s)}{e(s)} = K_\mathrm{P} + K_\mathrm{I} \cdot \frac{1}{s} + K_\mathrm{D} \cdot s \tag{33}$$

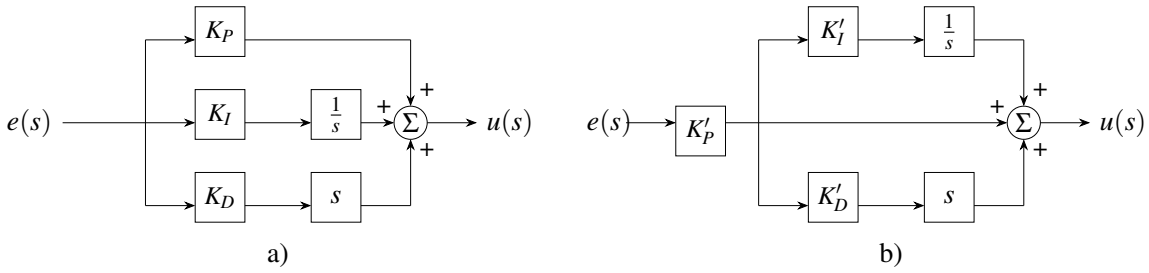

Figure 14: Block diagram of the a) parallel and b) standard implementation of a PID controller

The proportional term in the controller responds linearly to the error value. Since an error signal is required to produce any control action, the proportional action will not drive the output to the desired output, instead there will be a persistent steady-state error which is inversely proportional to the magnitude of the gain. The integral term accumulates past errors and effectively eliminates steady state error, however it can produce setpoint overshoot and contribute to oscillations. The derivative term 'anticipates' errors by responding to the instantaneous rate of change of the error signal. An ideal derivative action is non-causal,

meaning that knowledge about the future state of the system is required to compute the current action. However, this is not possible to implement in real systems. Instead, a low-pass filter is employed to calculate a derivative term based on past values, this also has the effect of filtering out high frequency noise which can be amplified by the derivative term and produce undesirable control action. The derivative branch has the effect of reducing overshoot and settling time (Kiam Heong Ang, Chong & Yun Li, 2005).

Variants of the PID controller exist where one or more control actions are not included in the controller. Commonly, PI controllers are used when the input signal is noisy, which can cause the derivative term to enforce a strong action which might be undesirable.

Additional components can optionally be added to the PID controller to negate undesired behaviour. One such feature is anti-windup, which is added to the integral control branch to reduce the effect of integral windup. Integral windup occurs when a desired output u exceeds the maximum allowable output value $u_{\max}$ for a prolonged period of time, possibly due to a setpoint which exceeds a physical limit. This results in a large accumulated control action in the integral branch. If the setpoint were then to be changed to a value lower than $u_{\max}$, the integral control action would still be positive until the negative error signal was sustained long enough for the integral branch to reach a critical limit where the output can begin decreasing (Ogata, 2022). There are several strategies to reduce the effect of integral windup; the method relevant to this thesis is *conditional integration* which essentially 'turns-off' the integral branch of the controller if the output is detected to be saturated, stopping it from accruing the overshoot from the error value.

3 Simulation Models

The goal of the simulations are to test the effect of excitation system control variants (P, PI, and PID) on the small-signal stability of the coupled synchronous machine and grid forming inverter. This is carried out by EMT simulations in the MATLAB Simulink environment, which is a computational method of simulating electrical systems on in a very short 'transient' timescale. To this end, two simulation models were created: an 'infinite bus' model, and an 'integrated' model. The infinite bus model is used to verify the synchronous generator against the analytical model to be developed in Chapter 4, and to verify the tuning of the PI and PID controllers. The integrated model is used to perform the small-signal stability tests.

3.1 Infinite Bus Model

Synchronous generators are typically modelled within an *infinite bus* (Kundur, 2009), which consists of the generator connected to an ideal stiff grid through a line with impedance This approximates a single machine connected to large transmission network while simplifying calculations associated with their interaction.

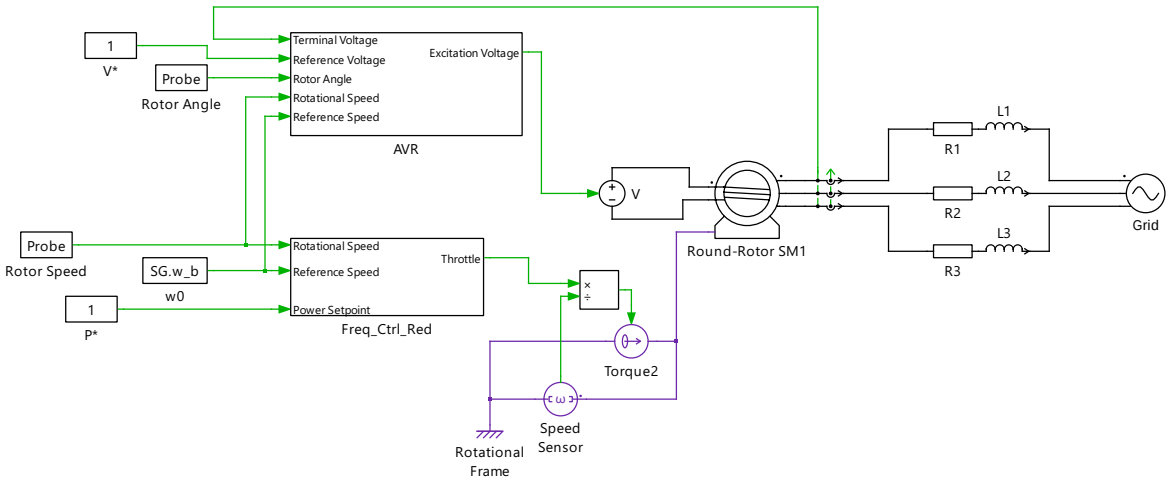

Figure 15: PLECS schematic of the infinite bus model topology

To create the model, a set of synchronous generator parameters presented in Table 1 are used as inputs to a *Round Rotor Synchronous Machine* block, which is a standard block in the PLECS library. This block takes a voltage input for the rotor field windings and an input for the rotor torque. The output of the block are the electrical terminal connections with voltage E_t. Excitation and frequency control systems were developed in PLECS, which is a third-party Matlab plugin, and provide the signal inputs into the generator block. The electrical output, at the nominal 27 kV voltage level, connects to an ideal three-phase voltage source representing a stiff grid, through a line with impedances given in Table 1. While ideally the model would include a Delta-wye transformer connecting the generator to the

grid at 110 kV, issues in the standard PLECS transformer block prevented the simulation from running. It was decided that the effect of the generator should be negligible on the small-signal stability, especially regarding rotor angle stability which is the focus of this research, so the transformer was neglected and the system modelled at 27 kV. The high-level implementation of the model in PLECS is shown in Figure 15.

Table 1: Physical parameters of infinite bus model

Synchronous Machine (Zhang et al., 2023)	
Base	$S = 1.4$ GVA, $E_\mathrm{t} = 27$ kV, $\cos(\phi) = 0.8$, $f = 50$ Hz
Rotor	$R_\mathrm{fd} = 0.0014$ pu, $R_\mathrm{1d} = 0.0238$ pu, $R_\mathrm{1q} = 0.0133$ pu, $R_\mathrm{2q} = 0.0364$ pu, $L_\mathrm{fd} = 0.1264$ pu, $L_\mathrm{1d} = 0.0436$ pu, $L_\mathrm{1q} = 0.4565$ pu, $L_\mathrm{2q} = 0.0472$ pu
Stator	$R_\mathrm{a} = 0.0021$ pu, $L_\sigma = 0.228$ pu, $L_\mathrm{ad} = 2.402$ pu
Mechanical	$J\ (= 2H)\ = 10$ pu
Transmission System	
Line	$R' = 0.002\ \Omega/\mathrm{km}$[1], $X' = 0.0.016\ \Omega/\mathrm{km}$[1], Length= 10 km $R = 0.0382$ pu, $X = 0.3078$ pu
Grid	$E_\mathrm{G} = 0.98$ pu

[1] Impedance converted to 27 kV voltage level from 110 kV given in source (Oeding & Oswald, 2016)

3.1.1 Excitation Control Implementation

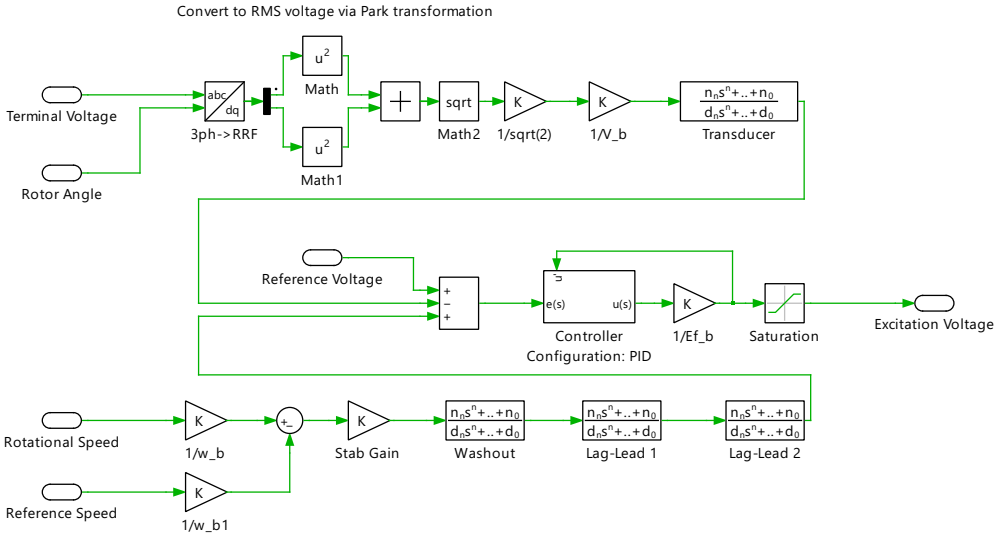

Figure 16: Generator excitation system as modelled in PLECS

The excitation system as modelled in Figure 8 is implemented in PLECS as per Figure 16. The three-phase terminal voltage is passed through a Park transformation block to obtain a d- and q- phasor. The RMS voltage is then obtained by computing the magnitude of the phasor and dividing by $\sqrt{2}$, before being converted into a per-unit value, representing E_t. This is then passed to a transfer function modelling a transducer delay with time constant T_R

before being subtracted from the reference voltage to form an error signal. This connects to a configurable block which can act as a P, PI or PID controller. The control action is then converted to volts and passed through a saturation block enforcing a maximum and minimum voltage $E_{\text{fd,max}}$ and $E_{\text{fd,min}}$, as per Table 3. $E_{\text{fd,max}}$ is chosen as a reasonable value based on the range of acceptable values presented in the IEEE recommended practices (IEEE, 2016). $E_{\text{fd,min}}$ is set to 0 V, which is not typical within the recommended practices. This was chosen as the synchronous machine model in PLECS was observed to only be influenced by the magnitude of the excitation voltage, not the sign. This meant that reducing the excitation voltage from 0 to -1 V increased the terminal voltage rather than decreasing it. This reduced saturation bound can have a significant effect on the excitation system behaviour, potentially altering the stability characteristics of the system. We will see in Section 5.1 that instability is observed in situations where both the exciter does and does not reach saturation, so this limitation does not completely overshadow the results. However, it is clear that having a limited lower saturation bound reduces the responsiveness of the system, which may mask fast-acting and potentially destabilising interactions between the generator and inverter.

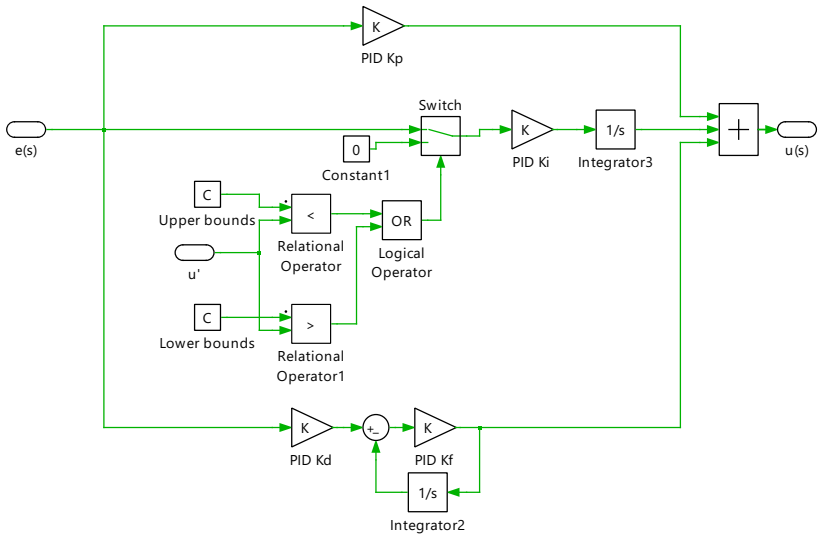

Figure 17: Implementation of the PID controller in PLECS

In the PLECS model, the error signal can additionally be augmented by a PSS which accepts a nominal reference speed $\omega^* = \omega_0$ and a measurement of the rotor speed ω_r. The two quantities are converted to per-unit values and compared to form a speed error $\Delta\omega$. This is then passed through the stabiliser gain, washout filter and the lag-lead filter. Note that the PSS is disabled for the infinite bus simulations.

The PI and PID controllers are implemented in the parallel form. The integral components have a conditional trigger which detects when the exciter output is saturated and disconnects the error signal from the integrator in order to avoid integral windup. The derivative is implemented with a filter K_{f} over which an integrator is negatively fed-back, which is algebraic

identical to a derivative action (O'Dwyer, 2009). The PID controller is shown in Figure 17; the PI controller is identical in structure without the derivative branch, and the P controller consists of a single inline gain.

Unfortunately, obtaining a stable implementation of the infinite bus model with an ideal parameter set in PLECS proved challenging, particularly at the start of the simulation where the start-up sequence does not have the generator start in-phase with the grid, but rather with some significant phase difference, requiring the system to equalise from a heavily perturbed state. With the nominal saturation bounds, the system would come close to stabilising, but oscillations would persist and eventually grow, leading to instability. To resolve this, the system was started with a modified maximum saturation bound of $E'_{\text{fd,max}} = 8$ pu, and then once the system stabilised, the bounds were increased to the nominal $E_{\text{fd,max}} = 30$ pu. Ultimately, this change had no effect on the step response, but it may point to underlying issues in the model which cause a lack of robustness. This lack of the robustness could be due to the neglected Thévenin equivalent impedance in the infinite bus model, which severely reduces the total impedance between the generator and the grid. However, including the Thévenin impedance within the current model did not improve stability, and more investigation is required in future work.

3.1.2 Frequency Control Implementation

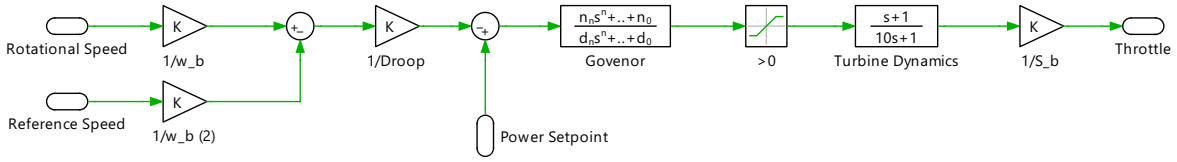

Figure 18: Frequency control implementation in PLECS

The generator frequency control is implemented in PLECS as per Figure 3 b). A speed error signal $\Delta\omega$ is generated before being passed through the frequency droop gain. This is compared to the power setpoint P^* to form a torque setpoint, which is then fed into a transfer function modelling the governor time delay with time constant T_g. A saturation block limits the output to be greater than zero, as to avoid unintended operation. This signal is then sent to a transfer function representing the turbine dynamics, as adapted from (Markovic et al., 2021) with time constant T_G. Finally, the signal is converted to a torque value by multiplying by the power base and dividing by a measurement of the shaft speed.

3.2 Integrated Model

In the integrated model, the generator is connected to a grid forming inverter model with a parallel shared passive load. A single line diagram of the model is presented in Figure 19.

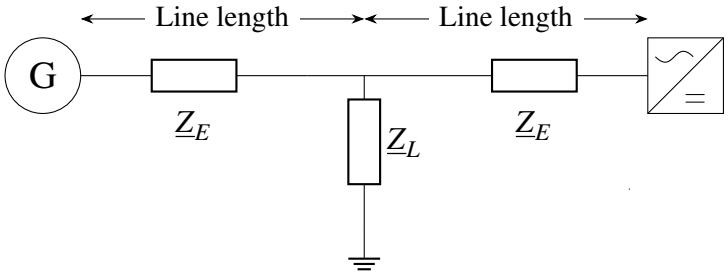

Figure 19: Single line diagram of the integrated model

Table 2: Physical parameters of the integrated model

Synchronous Generator	
As per Table 1	
Grid Forming Inverter(Zhang et al., 2023)	
Base	$S = 1.4$ GVA, $E_\mathrm{t} = 27$ kV, $\cos(\phi) = 0.8$, $f = 50$ Hz
Line	$R_\mathrm{t} = 0.0281$ pu
Filter	$C_\mathrm{f} = 0.0262$, $R_\mathrm{f} = 0.1687$, $L_\mathrm{t} = 0.088$ pu
Transmission System	
Line	$R' = 16.6 \cdot 10^{-3}$ Ω/km[1], $X' = 0.0013$ Ω/km[1], length= 100 km $R = 0.0320$ pu, $X = 0.256$ pu

[1] Impedance converted to 27 kV voltage level from 380 kV given in the source (Oeding & Oswald, 2016)

The grid forming inverter is modelled natively in the Matlab Simulink environment. The control structure implemented is based on a model developed in (Strunk & Mertens, 2023). Two droop control paths depicted in Figure 20 create a voltage reference signal which is fed to a voltage control block. The droop paths are *P*-ω droop and *Q*-*V* droop. The voltage control block calculates a reference current which is sent to a current control block to create voltage signals which are emulated in PLECS. Finally, the output signal is filtered through an LC filter with a line inductance L_t and resistance R_t, with a parallel capacitance C_f and resistance R_f. The output is then measured and fed back into each control path.

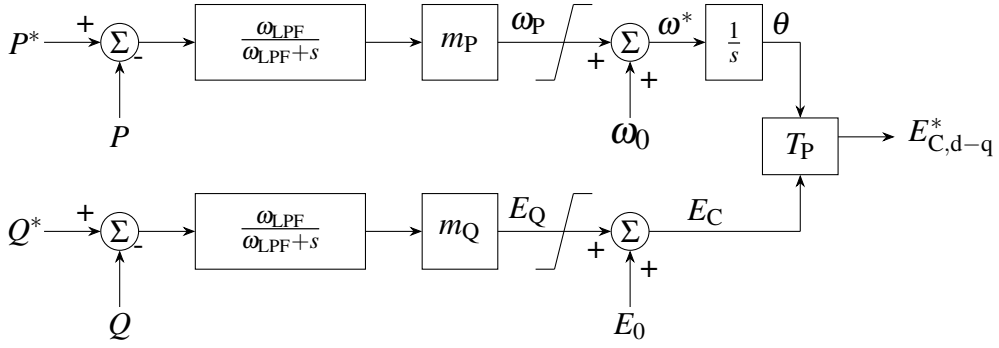

Figure 20: Droop control paths of the grid forming inverter (Strunk & Mertens, 2023)

Table 3: Generator and inverter control parameters

Synchronous Generator	
Excitation System	$T_R = 0.02$ s [1] $K_P = 210$ [1], $E_{fd,max} = 30$ pu, $E_{fd,min} = 0$ pu
PSS [1]	$K_G = 30$, $T_W = 10$ s, $T_1 = 0.05$ s, $T_2 = 0.02$ s, $T_3 = 3$ s, $T_4 = 5.4$ s
Frequency Control	$T_g = 0.2$ s [1], $T_G = 10$ s [2], R=5%
Inverter	
Current Control	$K_{P,i} = 0.0344$ V/A
Voltage Control	$K_{P,v} = 0.189$ A/V, $K_{I,v} = 833.3$ A/V $\cdot$ s
Droop	$m_P = 11.22$ rad/GW, $m_Q = 787.34$ V/GVAr, $f_{LPF} = 5$ Hz

[1] Zhang et al., 2023
[2] Markovic et al., 2021

The control parameters for the inverter were derived using tuning methods with consideration for the application within this simulation. The voltage control uses a PI controller and was tuned using the symmetrical optimum method (Schröder & Böcker, 2021) with gains $K_{P,v}$ and $K_{I,v}$. The current control uses a P type controller and was tuned using the magnitude optimum method (Schröder & Böcker, 2021) with gain $K_{P,i}$. The LC filter parameters are taken from (Zhang et al., 2023), and their values, along with all control values for the model, are presented in Table 3.

The model is integrated with the synchronous generator in PLECS. The generator implementation remains the same as the infinite bus model. The system up until the generators feed-in lines are depicted in Figure 21.

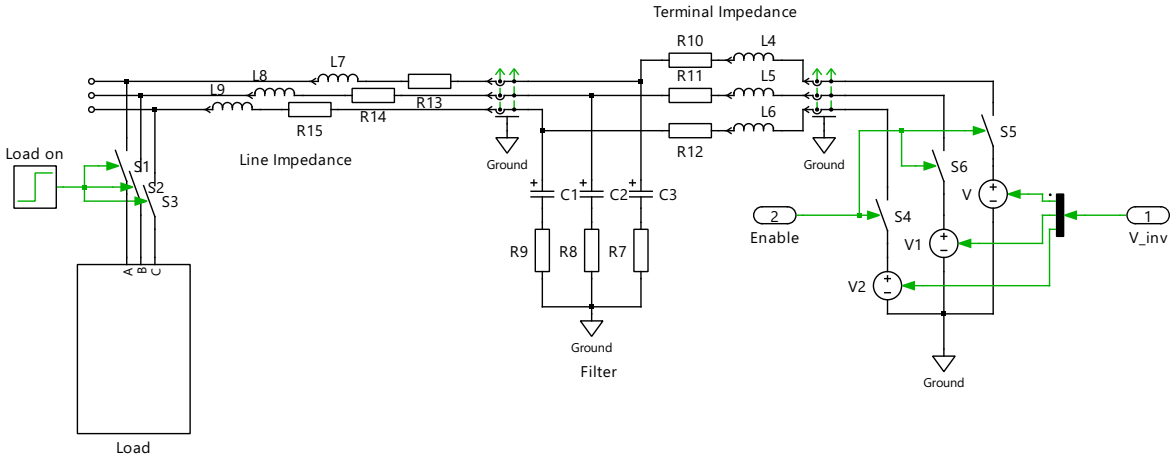

Figure 21: Grid forming inverter integration into synchronous generator model

The shared load is passive and consists of resistors and inductors. The impedance values are

chosen to produce as power factor of 0.8, without considering the impedance of the transmission lines. The load is varied over the simulation time to achieve two goals: firstly to bring the system up to nominal operating conditions while causing minimal transient impact, and secondly to subject the system to a transient step load at a given time. Starting the system and achieving nominal power without causing transient disturbance proved difficult, especially at reduced line lengths. A solution was implemented by employing variable resistors and inductors and following the described start-up procedure:

1. At $t = 0$ s start generator with $P^*_{\text{gen}} = 0$ and the inverter disconnected at switches S4, S5 and S6 (as per Figure 21) .
2. At $t = 2$ s connect and enable inverter with $P^*_{\text{inv}} = 0$.
3. At $t = 6$ s linearly ramping the power setpoints P^*_{gen} and $P^*_{\text{inv}} = 0$ over 15 seconds
4. At $t = 6.1$ s ramp the load according to the function

$$Z(t) = Z_0 \left(1 + (\alpha - 1) \frac{B(R - (t - t_0))}{R((t - t_0) + B)} \right), \quad t_0 \leq t \leq R \tag{34}$$

   where Z_0 is the nominal load, t_0 is the ramp start time in seconds, R ramp duration in seconds, α is an initial load factor (such that $Z(t_0) = \alpha Z_0$), and B is a dimensionless shape factor. For this model $\alpha = 30$, $R = 15$ seconds, and $B = 0.8$.
5. At $t = 21.1$ s stop ramping and allow system to settle.

The system is considered settled when the power of the generator and inverter are equal. At which point the system can be subjected to a 10% step load by connecting a parallel impedance, reducing the total effective load impedance and increasing the system current. A typical start-up and load step simulation is shown in Figure 22

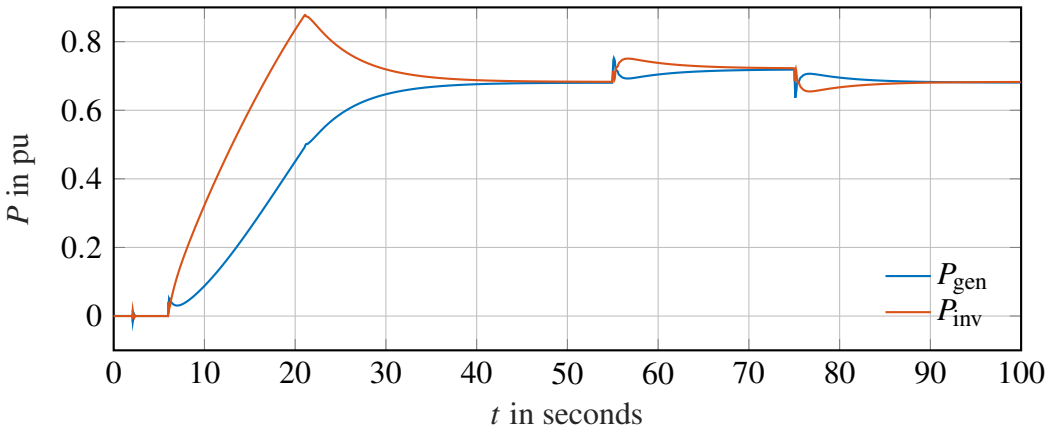

Figure 22: A full simulation of the integrated model with a 100 km line length, $S = 1.3$ pu and 10% power step

4 Analytical Model of the Synchronous Generator

In order to tune the gain constants associated with the P, PI and, PID controllers for the EMT simulation, an analytical model of the synchronous machine must be derived. The generator is modelled connected to an infinite bus as per Figure 23, where $\underline{E}_{\mathrm{t}}$ is the terminal voltage, $\underline{Z}_{\mathrm{E}}$ is the equivalent line impedance, and $\underline{E}_{\mathrm{G}}$ is the grid voltage. The goal is to develop a single-input single-output (SISO) open-loop transfer function that represents the linearized dynamics of the synchronous machine, the excitation system, and the damper coils while connected to the infinite bus. This transfer function will then be used to apply analytical methods of PID tuning to derive optimal gain coefficients for the controller of the excitation system.

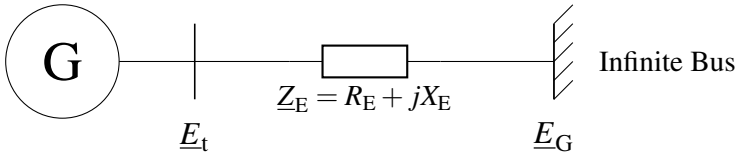

Figure 23: Generator connected to an infinite bus

It should be noted that, typically, an infinite bus representation should include a Thévenin equivalent impedance for the grid in line with the line impedance, but this was not included within this representation. The significance and impact of this are discussed in Chapter 6.

4.1 Model Parameters

The synchronous machine parameters are adopted from (Zhang et al., 2023). The generator is modelled with a nominal power of 1.4 GVA and a 27 kV nominal voltage, with these parameters forming the bases of the system per-unit values. The full set of parameters are given in Tables 1 and 3.

The line impedance is adopted from a 110 kV transmission line with $R' = 0.033\ \Omega/\mathrm{km}$, $X' = 0.266\ \Omega/\mathrm{km}$ (Oeding & Oswald, 2016), with the impedance being referred to the 27 kV voltage level and the line assumed to be 10 km long. The grid is assumed to have a voltage level of $E_{\mathrm{B}} = 0.98$ pu.

4.2 Analytical Model

The model derived in this section uses the method outlined in (Kundur, 2009). The model will be derived for a simple representation of a generator as a voltage source behind an impedance, extended to include the dynamics of the field circuit with damper coils, and then finally represented with a controllable excitation system. The result is a SISO transfer

function that takes the voltage set point E^* as an input, and gives the terminal voltage as measured by the excitation system transducer v_1 as an output, seen in Figure 8.

A generator is classically modelled as a voltage source $\underline{E}_\mathrm{A}$ behind an internal reactance X_d as represented in Figure 24. The generator voltage is chosen as the reference phasor and leads the infinite bus by angle δ.

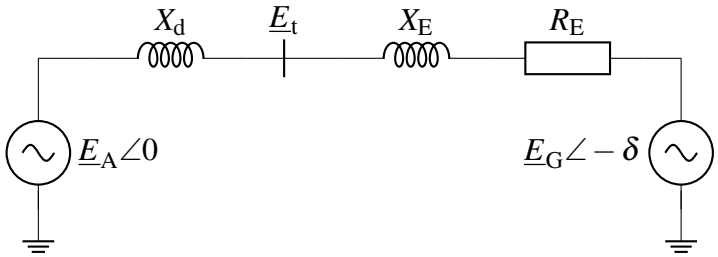

Figure 24: Synchronous machine as a voltage source behind an impedance connected to an infinite bus.

The power flow over the circuit is given by

$$\underline{S} = P + jQ = \underline{E}_\mathrm{A}\underline{I}^* = \frac{\underline{E}_\mathrm{A}(\underline{E}_\mathrm{A} - \underline{E}_\mathrm{G})}{R_\mathrm{E} + jX_\mathrm{T}}. \tag{35}$$

If we ignore resistance in the stator, then the air gap power P_e is equal to the system power P, which in a per-unit system, is also equal to the air gap torque τ_e. Thus,

$$\tau_\mathrm{e} = P = \frac{E_A(E_A R_\mathrm{E} - E_\mathrm{G} R_\mathrm{E}\cos(\delta) + E_\mathrm{G} X_\mathrm{T}\sin(\delta))}{R_\mathrm{E}^2 + X_\mathrm{T}^2}, \tag{36}$$

which can be linearized around a nominal operating point by

$$\Delta\tau_\mathrm{e} = \frac{\partial\tau_\mathrm{e}}{\partial\delta}\Delta\delta = \frac{E_\mathrm{A}E_\mathrm{G}(X_\mathrm{T}\cos(\delta_0) + R_\mathrm{E}\sin(\delta_0))}{X_\mathrm{T}}\Delta\delta = K_\mathrm{S}\Delta\delta, \tag{37}$$

where K_S is the synchronising torque constant. By substituting this torque relation into a linearized form of the swing equation from Equation 7, we can obtain

$$\Delta\dot{\omega}_\mathrm{r} = \frac{1}{2H}(\Delta\tau_\mathrm{m} - K_\mathrm{S}\Delta\delta - K_\mathrm{D}\Delta\omega_\mathrm{r}). \tag{38}$$

Given that the rate of change in load angle $\Delta\dot{\delta} = \Delta\omega_\mathrm{r}$, this expression can be written in the

matrix form

$$\begin{bmatrix} \Delta\dot{\omega}_{\mathrm{r}} \\ \Delta\dot{\delta} \end{bmatrix} = \begin{bmatrix} -\dfrac{K_{\mathrm{D}}}{2H} & -\dfrac{K_{\mathrm{S}}}{2H} \\ \omega_0 & 0 \end{bmatrix} \begin{bmatrix} \Delta\omega_{\mathrm{r}} \\ \Delta\delta \end{bmatrix} + \begin{bmatrix} \dfrac{1}{2H} \\ 0 \end{bmatrix} \Delta\tau_{\mathrm{m}}. \tag{39}$$

This is a representation of the generator dynamics in the form $\dot{\vec{x}} = \mathbf{A}\vec{x} + \mathbf{B}\vec{u}$ and can thus be used as a state space formulation of the system. However, this does not account for any dynamics associated with the field circuit. To account for these, we must add additional state variables to our model which express the flux linkage associated with each field coil. The chosen synchronous generator model consists of a primary field winding with flux linkage Ψ_{fd}, one d-axis damper coil and 2 q-axis damper coils with flux linkages $\Psi_{1\mathrm{d}}$, $\Psi_{1\mathrm{q}}$ and $\Psi_{2\mathrm{q}}$ respectively. This can be achieved by deriving expressions for the field circuit in terms of state variables.

The equivalent d- and q- axis circuits for the rotor are shown in Figure 25.

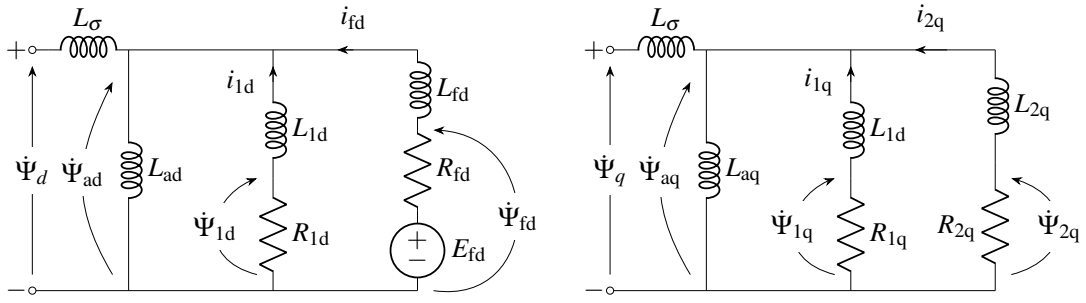

Figure 25: Field winding circuit for the a) d-axis and b) q-axis (Kundur, 2009)

Given that voltage is equal to the rate of change of magnetic flux linkage we can derive voltage relations for the circuits by

$$\begin{aligned} \dot{\Psi}_{\mathrm{fd}} &= \frac{\omega_0 R_{\mathrm{fd}}}{L_{\mathrm{ad}}} E_{\mathrm{fd}} - \omega_0 R_{\mathrm{fd}} i_{\mathrm{fd}} \\ \dot{\Psi}_{1\mathrm{d}} &= -\omega_0 R_{1\mathrm{d}} i_{1\mathrm{d}} \\ \dot{\Psi}_{1\mathrm{q}} &= -\omega_0 R_{1\mathrm{q}} i_{1\mathrm{q}} \\ \dot{\Psi}_{2\mathrm{q}} &= -\omega_0 R_{2\mathrm{q}} i_{2\mathrm{q}}, \end{aligned} \tag{40}$$

where E_{fd} is the exciter output voltage in the reciprocal per-unit system of the exciter. Also given that the flux linkage is the product of inductance and current, expressions for the cur-

rent in each field coil can be derived from Figure 25 by

$$\begin{aligned} i_{\mathrm{fd}} &= \frac{1}{L_{\mathrm{fd}}}(\Psi_{\mathrm{fd}} - \Psi_{\mathrm{ad}}) \\ i_{\mathrm{1d}} &= \frac{1}{L_{\mathrm{1d}}}(\Psi_{\mathrm{1d}} - \Psi_{\mathrm{ad}}) \\ i_{\mathrm{1q}} &= \frac{1}{L_{\mathrm{1q}}}(\Psi_{\mathrm{1q}} - \Psi_{\mathrm{aq}}) \\ i_{\mathrm{2q}} &= \frac{1}{L_{\mathrm{2q}}}(\Psi_{\mathrm{2q}} - \Psi_{\mathrm{aq}}). \end{aligned} \tag{41}$$

Re-arranging 41 and equating the mutual flux linkage terms Ψ_{ad} and Ψ_{aq} we obtain

$$\begin{aligned} \Psi_{\mathrm{ad}} &= L'_{\mathrm{ad}}\left(-i_{\mathrm{d}} + \frac{\Psi_{\mathrm{fd}}}{L_{\mathrm{fd}}} + \frac{\Psi_{\mathrm{1d}}}{L_{\mathrm{1d}}}\right) \\ \Psi_{\mathrm{aq}} &= L'_{\mathrm{aq}}\left(-i_{\mathrm{q}} + \frac{\Psi_{\mathrm{1q}}}{L_{\mathrm{2q}}} + \frac{\Psi_{\mathrm{2q}}}{L_{\mathrm{2q}}}\right), \end{aligned} \tag{42}$$

where L' represents the total equivalent inductance in each circuit by

$$L'_{ad} = \frac{1}{\frac{1}{L_{ad}} + \frac{1}{L_{fd}} + \frac{1}{L_{1d}}} \quad L'_{aq} = \frac{1}{\frac{1}{L_{aq}} + \frac{1}{L_{1q}} + \frac{1}{L_{2q}}}. \tag{43}$$

The stator voltages can be defined in terms of flux linkages in the d- and q-axis (ignoring stator transients and speed variation terms) by

$$\begin{aligned} E_{\mathrm{td}} &= -R_{\mathrm{a}} i_{\mathrm{d}} + (L_{\sigma} i_{\mathrm{q}} - \Psi_{\mathrm{aq}}) \\ E_{\mathrm{tq}} &= -R_{\mathrm{a}} i_{\mathrm{q}} - (L_{\sigma} i_{\mathrm{d}} - \Psi_{\mathrm{ad}}) \end{aligned} \tag{44}$$

where R_{a} is the phase resistance of the stator. These voltages can also be calculated from the network side by first resolving the system voltages to d- and q-components

$$\underline{E}_{\mathrm{t}} = E_{\mathrm{td}} + jE_{\mathrm{tq}} \qquad \underline{E}_{\mathrm{G}} = E_{\mathrm{Gd}} + jE_{\mathrm{Gq}}, \tag{45}$$

and then solving the constraint equations dictated by Figure 24 to get

$$\begin{aligned} E_{\mathrm{td}} &= R_{\mathrm{E}} i_{\mathrm{d}} - X_{\mathrm{E}} i_{\mathrm{q}} + E_{\mathrm{Gd}} \\ E_{\mathrm{tq}} &= R_{\mathrm{E}} i_{\mathrm{q}} - X_{\mathrm{E}} i_{\mathrm{d}} + E_{\mathrm{Gq}}. \end{aligned} \tag{46}$$

By equating Equations 44 and 46 and substituting the air gap flux linkage relations from

Equation 42 we can express the d- and q-axis currents in terms of state variables

$$\begin{aligned} i_{\mathrm{d}} &= \frac{X_{\mathrm{Tq}}\left(E''_{\mathrm{tq}} - E_{\mathrm{G}}\cos(\delta)\right) - R_{\mathrm{T}}\left(E''_{\mathrm{td}} + E_{\mathrm{G}}\sin(\delta)\right)}{R_{\mathrm{T}}^2 + X_{\mathrm{Td}}X_{\mathrm{Tq}}} \\ i_{\mathrm{q}} &= \frac{R_{\mathrm{T}}\left(E''_{\mathrm{tq}} - E_{\mathrm{G}}\cos(\delta)\right) + X_{\mathrm{Td}}\left(E''_{\mathrm{td}} + E_{\mathrm{G}}\sin(\delta)\right)}{R_{\mathrm{T}}^2 + X_{\mathrm{Td}}X_{\mathrm{Tq}}}, \end{aligned} \tag{47}$$

where

$$E''_{\mathrm{td}} = L'_{\mathrm{ad}}\left(\frac{\Psi_{1\mathrm{q}}}{L_{1\mathrm{q}}} + \frac{\Psi_{2\mathrm{q}}}{L_{2\mathrm{q}}}\right) \qquad E''_{\mathrm{tq}} = L'_{\mathrm{aq}}\left(\frac{\Psi_{\mathrm{fd}}}{L_{\mathrm{fd}}} + \frac{\Psi_{1\mathrm{d}}}{L_{1\mathrm{d}}}\right).$$

We may then begin linearizing our equations around a nominal condition to form the system matrix. All m_i, n_i and a_{ij} coefficients are given in Appendix 1.

First we can express our d- and q-axis currents by

$$\begin{aligned} \Delta i_{\mathrm{d}} &= m_1\Delta\delta + m_2\Delta\Psi_{\mathrm{fd}} + m_3\Delta\Psi_{1\mathrm{d}} + m_4\Delta\Psi_{1\mathrm{q}} + m_5\Delta\Psi_{2\mathrm{q}} \\ \Delta i_{\mathrm{q}} &= n_1\Delta\delta + n_2\Delta\Psi_{\mathrm{fd}} + n_3\Delta\Psi_{1\mathrm{d}} + n_4\Delta\Psi_{1\mathrm{q}} + n_5\Delta\Psi_{2\mathrm{q}}. \end{aligned} \tag{48}$$

Substituting this into Equation 42 and linearizing results in

$$\begin{aligned} \Delta\Psi_{\mathrm{ad}} =& -m_1L'_{\mathrm{ad}}\Delta\delta + L'_{\mathrm{ad}}\left(\frac{1}{L_{\mathrm{fd}}} - m_2\right)\Delta\Psi_{\mathrm{fd}} \\ &+ L'_{\mathrm{ad}}\left(\frac{1}{L_{1\mathrm{d}}} - m_3\right)\Delta\Psi_{1\mathrm{d}} - m_4L'_{\mathrm{ad}}\Delta\Psi_{1\mathrm{q}} - m_5L'_{\mathrm{ad}}\Delta\Psi_{2\mathrm{q}} \\ \Delta\Psi_{\mathrm{aq}} =& -n_1L'_{\mathrm{aq}}\Delta\delta + L'_{\mathrm{aq}}\left(\frac{1}{L_{1\mathrm{q}}} - n_4\right)\Delta\Psi_{1\mathrm{q}} \\ &+ L'_{\mathrm{aq}}\left(\frac{1}{L_{2\mathrm{q}}} - n_5\right)\Delta\Psi_{2\mathrm{q}} - n_2L'_{\mathrm{aq}}\Delta\Psi_{\mathrm{fd}} - n_3L'_{\mathrm{aq}}\Delta\Psi_{1\mathrm{d}}. \end{aligned} \tag{49}$$

Substituting this into the machine torque relation, the air-gap torque τ_{e} is defined as

$$\tau_{\mathrm{e}} = \Psi_{\mathrm{ad}}i_{\mathrm{q}} - \Psi_{\mathrm{aq}}i_{\mathrm{d}}. \tag{50}$$

Linearizing and substituting Equations 48 and 49 gives an expression of the air-gap torque in terms of each system variable. This can be substituted into a linearized form of the swing

equation described in Equation 7 to give

$$\begin{aligned}\Delta\dot{\omega}_{\mathrm{r}} &= \frac{1}{2H}(\Delta\tau_{\mathrm{m}} - \Delta\tau_{\mathrm{e}} - K_{\mathrm{D}}\Delta\omega_{\mathrm{r}}) \\ &= a_{11}\Delta\omega_{\mathrm{r}} + a_{12}\Delta\delta + a_{13}\Delta\Psi_{\mathrm{fd}} + a_{14}\Delta\Psi_{1\mathrm{d}} + a_{15}\Delta\Psi_{1\mathrm{q}} + a_{16}\Delta\Psi_{2\mathrm{q}} + b_{11}\Delta\tau_{\mathrm{m}}.\end{aligned} \tag{51}$$

Equations of a similar form can be obtained by substituting the air-gap mutual flux linkages from Equation 49 into the current relations from Equation 41 to get linearized expressions for each coil flux linkage. The result is a state equation of the form

$$\begin{bmatrix} \Delta\dot{\omega}_{\mathrm{r}} \\ \Delta\dot{\delta} \\ \Delta\dot{\Psi}_{\mathrm{fd}} \\ \Delta\dot{\Psi}_{1\mathrm{d}} \\ \Delta\dot{\Psi}_{1\mathrm{q}} \\ \Delta\dot{\Psi}_{2\mathrm{q}} \end{bmatrix} = \begin{bmatrix} a_{11} & a_{12} & a_{13} & a_{14} & a_{15} & a_{16} \\ a_{21} & 0 & 0 & 0 & 0 & 0 \\ 0 & a_{32} & a_{33} & a_{34} & a_{35} & a_{36} \\ 0 & a_{42} & a_{43} & a_{44} & a_{45} & a_{46} \\ 0 & a_{52} & a_{53} & a_{54} & a_{55} & a_{56} \\ 0 & a_{62} & a_{63} & a_{64} & a_{65} & a_{66} \end{bmatrix} \begin{bmatrix} \Delta\omega_{\mathrm{r}} \\ \Delta\delta \\ \Delta\Psi_{\mathrm{fd}} \\ \Delta\Psi_{1\mathrm{d}} \\ \Delta\Psi_{1\mathrm{q}} \\ \Delta\Psi_{2\mathrm{q}} \end{bmatrix} + \begin{bmatrix} b_{11} & 0 \\ 0 & 0 \\ 0 & b_{32} \\ 0 & 0 \\ 0 & 0 \\ 0 & 0 \end{bmatrix} \begin{bmatrix} \Delta\tau_{\mathrm{m}} \\ \Delta E_{\mathrm{fd}} \end{bmatrix}. \tag{52}$$

Equation 52 represents the dynamics of the synchronous machine within an infinite bus, with an allowance for changes in the excitation voltage ΔE_{fd}. However, this does not take into account the dynamics of the excitation system and its relationship to the voltage setpoint E^*, as well as the explicit relationship to the terminal voltage E_{t}. For this we must develop an output matrix relating these two variables. The block diagram of an excitation system is shown in Figure 8; the terminal voltage is taken as an input, read via a transducer with an associated time constant T_{R} and compared against the reference voltage before the signals enter the controller. Since we are considering the small-signal stability we can neglect the saturation block.

Given the expression for the terminal voltage in the d- and q- axis as per Equation 45, the terminal voltage can be linearized around an initial operating point by

$$\Delta E_{\mathrm{t}} = \frac{E_{\mathrm{td0}}}{E_{\mathrm{t0}}}\Delta E_{\mathrm{td}} + \frac{E_{\mathrm{tq0}}}{E_{\mathrm{t0}}}\Delta E_{\mathrm{tq}}. \tag{53}$$

Additionally, the d- and q- axis voltages from Equation 46 can be linearized and substituted into the terminal voltage to give

$$\Delta E_{\mathrm{t}} = K_1\Delta\delta + K_2\Delta\Psi_{\mathrm{fd}} + K_3\Delta\Psi_{1\mathrm{d}} + K_4\Delta\Psi_{1\mathrm{q}} + K_5\Psi_{2\mathrm{q}}. \tag{54}$$

Within our state space formulation, this expression for ΔE_t will form the basis of the output matrix $\mathbf{C}$. We now have a state space system with a set of 6 state variables, a plant matrix, an input matrix, and an output matrix. Assuming a constant torque, $\Delta\tau_\mathrm{m} = 0$, the system can be solved into a transfer function $H'(s)$ which maps the terminal voltage as an input to the excitation voltage ΔE_fd as an output

$$\frac{\Delta E_\mathrm{fd}(s)}{\Delta E_\mathrm{t}(s)} = H'(s). \tag{55}$$

To represent the voltage as read by the transducer we must multiply by the associated transducer time delay

$$\frac{\Delta E_\mathrm{fd}(s)}{\Delta v_1(s)} = H'(s)\frac{1}{1+sT_\mathrm{R}} = H(s). \tag{56}$$

Without a controller, the excitation voltage can be expressed as

$$E_\mathrm{fd} = E^* - v_1. \tag{57}$$

Since we are interested in the open-loop transfer function the contribution of v_1 is not considered. Thus, the final transfer function is

$$\frac{\Delta E^*(s)}{\Delta v_1(s)} = H(s). \tag{58}$$

Given the values in Table 4.2 this is be evaluated to

$$\frac{0.02s^5 + 1417s^4 + 1.2\cdot 10^6 s^3 + 1.4\cdot 10^8 s^2 + 1.3\cdot 10^9 s + 7.1\cdot 10^9}{0.02s^7 + 1273s^6 + 1.1\cdot 10^7 s^5 + 6.9\cdot 10^8 s^4 + 9.6\cdot 10^9 s^3 + 9.1\cdot 10^{10} s^2 + 5.6\cdot 10^{11} s + 1.2\cdot 10^{12}}. \tag{59}$$

4.2.1 Model Verification

To ensure that the tuning of the PI and PID controllers are optimal for the PLECS simulations, the behaviour and dynamics of the analytical model and the simulation model should be similar. To validate this, the behaviour of the two models were compared when subjected to an identical step response of $E^* : 1 \rightarrow 1.1$ pu. For the test, both the simulation and analytical model use an inline proportional controller with $K_\mathrm{P} = 210$ as per Table 3, with the analytical model connected in a closed loop topology with negative feedback.

Figure 26 shows the simulation and analytical model response to the voltage reference step. There was a significant difference in the steady state errors between the two signals; the

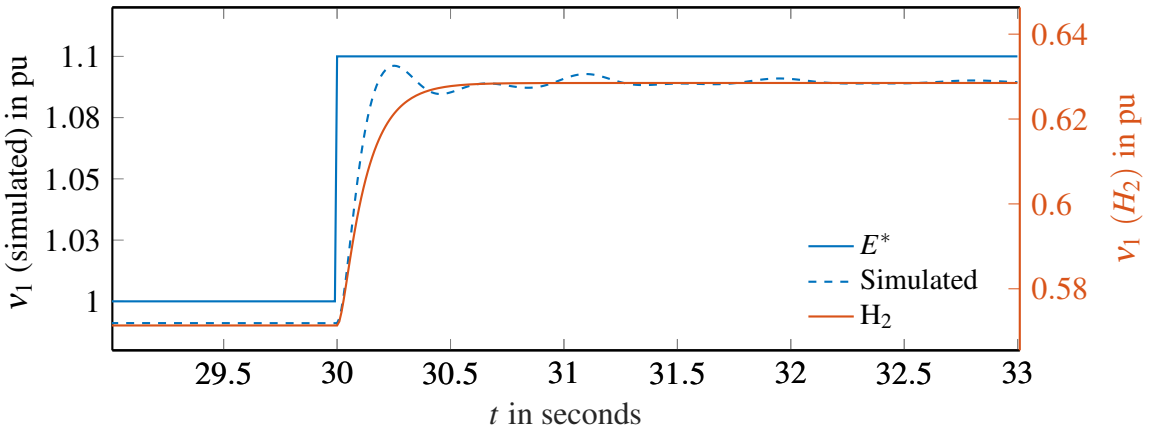

Figure 26: Step response of the infinite bus analytical model H_2 and simulated model with a P controller

analytical model was consistently approximately 57% of the reference value while the simulated model was a much more reasonable 99% of the reference value. The reason for this discrepancy is uncertain, and there is clearly and issue regarding the gain of the analytical model. However, by applying a corrective factor of $1/0.57$ to the analytical model signal, the shapes of the responses can be compared. It is clear that there are dynamics in the simulated model which are not represented in H_2, as seen by the overshoot and settling oscillations of the simulation, however this is unsurprising as the simulation has a far broader scope than what was considered in the analytical model derivation including non-linear elements. Future works should consider the noted discrepancy in steady state error and refine the model or test configuration to bring the output of the two models closer together.

4.3 Controller Tuning

The transfer function derived in Section 4.2 can be used within established analytical PID tuning methods. Two tuning procedures will be performed to develop optimum gain coefficients for a PI and PID controller. The P controller will use the gain given in (Zhang et al., 2023), which is the same source used for the synchronous generator parameters. Not only does this mean that the proportional gain value should already be tuned, but it also will act as a point of comparison to other literature results, as the given value of $K_\mathrm{P} = 210$ is similar across other studies which analyse synchronous generator and grid forming inverter interactions (Markovic et al., 2021) (Tayyebi et al., 2020).

Since the transfer function is of the 7^{th}-order it is helpful to reduce the system to a 2^{nd}-order system. This can be achieved by cancelling zero-pole pairs which occur within a small finite

region of each other. Employing this method, we can reduce the transfer function to

$$H_2(s) = \frac{1.103}{s^2 + 53.48s + 173.8}. \tag{60}$$

This reduced system model has very similar behaviour to the full 7$^{\text{th}}$ order model as shown in Figure 27.

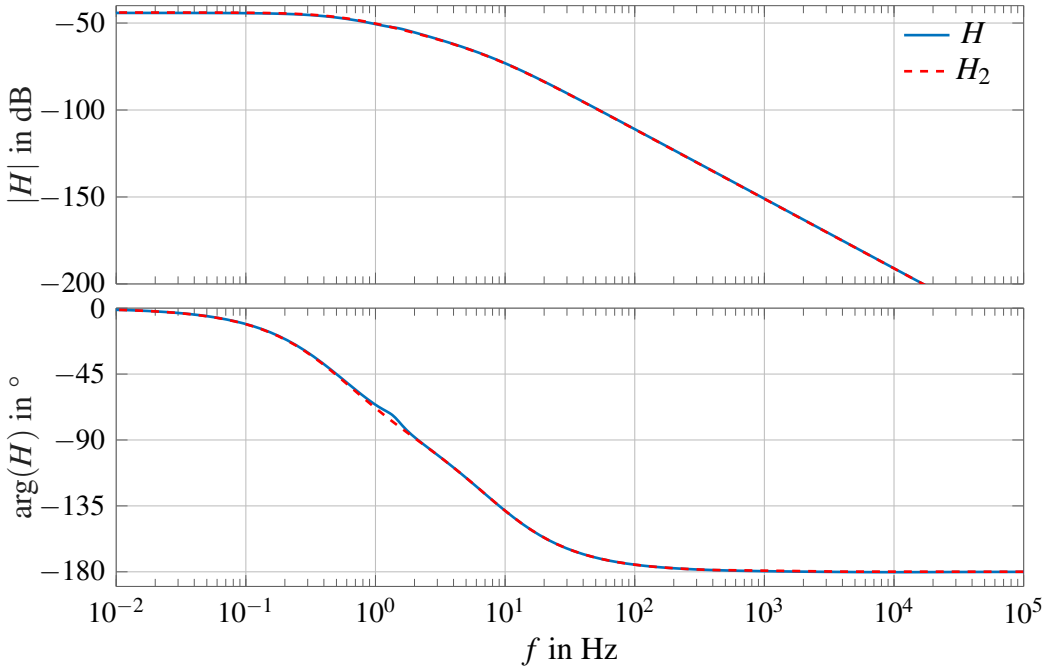

Figure 27: Bode plot of 7$^{\text{th}}$-order system transfer function and its 2$^{\text{nd}}$-order approximation

4.3.1 PI Controller

The symmetrical optimum (SO) tuning method first proposed by Kessler in 1958 is a popular tuning method, particularly for electrical drive applications (Landau & Voda, 1992). Fundamentally it attempts to create a symmetrical frequency response about a set amplitude pass frequency. It provides an analytical relationship between the transfer function and the PI gain constants, which can be fine-tuned using a single gain parameter a.

The plant transfer function must be expressed in the form

$$H_2(s) = \frac{V_S}{sT_1}\frac{1}{1+sT_2}, \quad T_1 > T_2. \tag{61}$$

Which, for the 2$^{\text{nd}}$ order infinite bus system, the characteristic values are

$$V_S = 0.0063 \text{ V} \quad T_1 = 0.288 \text{ s} \quad T_2 = 0.02 \text{ s}.$$

The SO PI controller takes the form

$$G(s) = V_{\mathrm{R}} \frac{1 + sT_{\mathrm{n}}}{sT_{\mathrm{n}}} \tag{62}$$

with coefficients related to the plant function by the analytical relations (Schröder & Böcker, 2021)

$$T_{\mathrm{n}} = a^2 T_2 \qquad V_{\mathrm{R}} = \frac{1}{a} \frac{T_1}{V_{\mathrm{S}} T_2}. \tag{63}$$

Typically, the tuning constant is set to $a = 2$, but this parameter can be adjusted to find the optimum performance for the system. a was initially tuned to the step response of the analytical model and then verified using the simulation model as discussed in Chapter 3.1. The parameter was then iteratively tuned in the simulation model against a step response to obtain the optimum performance. The final determined value was $a = 7$.

Thus, the gain constants of the parallel PI controller can be expressed as

$$\begin{aligned} K_{\mathrm{P}} &= \frac{1}{a} \frac{T_1}{V_{\mathrm{S}} T_2} = 323.8 \\ K_{\mathrm{I}} &= \frac{K_{\mathrm{P}}}{a^2 T_2} = 330.4 \ \mathrm{s}^{-1}. \end{aligned} \tag{64}$$

4.3.2 PID Controller

Internal model control (IMC) first proposed by Garcia and Morari (Garcia & Morari, 1982) is a control strategy that uses an internal model of the plant to predict system behaviour and design a controller that compensates for the plant dynamics. It incorporates the plant model directly into the controller definition to achieve the desired closed loop performance.

The method requires the plant transfer function be factorised in the form

$$H(s) = H_+(s) H_-(s) \tag{65}$$

where H_+ contains all time delays and right-half plane poles. This means that H_-^{-1} is stable by definition and contains no predictors. The controller is then defined as

$$G(s) = H_-^{-1}(s) \frac{1}{\varepsilon s + 1} \tag{66}$$

where the fractional term is a low pass filter defined by the tuning constant ε. Given the factorisation of the transfer function in Equation 61, the controller has the form

$$G(s) = \frac{(T_1 s + 1)(T_2 s + 1)}{V_{\mathrm{S}} \varepsilon s}. \tag{67}$$

Similarly to Section 4.3.1, the tuning constant ε was calibrated to a step response against the analytical model, and then iteratively tuned within the simulation to obtain the best controller behaviour. The final tuned value was $\varepsilon = 0.1$. The controller can then be converted to gain constants for a parallel PID controller by

$$\begin{aligned} K_\mathrm{P} &= \frac{T_1 + T_2}{V_\mathrm{S}\varepsilon} = 484.8 \\ K_\mathrm{I} &= \frac{1}{V_\mathrm{S}\varepsilon} = 1575.5\ \mathrm{s}^{-1} \\ K_\mathrm{D} &= \frac{T_1 T_2}{V_\mathrm{S}\varepsilon} = 9.1\ \mathrm{s} \end{aligned} \tag{68}$$

The filter gain K_f was determined using the Matlab PID tuner toolbox and found to be $K_\mathrm{f} = 4.4$.

4.3.3 Controller Verification

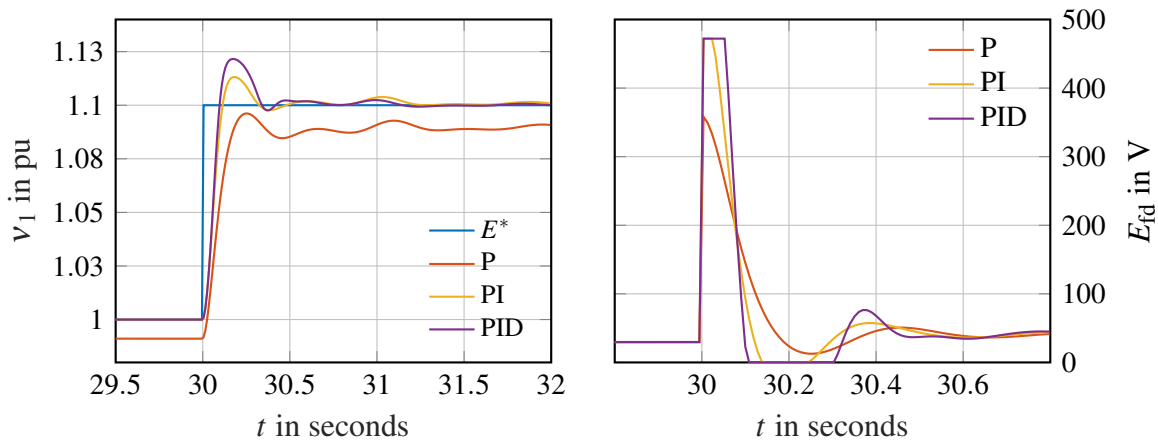

Figure 28: Comparison of P, PI and PID controller step response in an infinite bus and the excitation output

The behaviour of the PI and PID controllers should be verified within the infinite bus simulation model to ensure satisfactory behaviour within simulation conditions. Figure 28 shows the PI and PID controller compared to a P controller, subjected to a step response of $E^* : 1 \rightarrow 1.1$ pu, plotting the terminal voltage as read by the transducer v_1 as well as the excitation output. Firstly, it is noted that both the PI and PID controller reach the exciter saturation limit at the rising edge of the step, which introduces non-linearity and compromises a fair assessment of the controller's behaviour. However, saturation is only maintained in the PI and PID controllers for 0.02 and 0.05 s respectively, whereas the maximum terminal voltage for the controllers was reached 0.18 s after the step for both controllers. So while the controller behaviour is affected by the saturation, the effects should be minimal regarding at least the overshoot characteristics. Rise time and stability may be affected by the saturation.

Comparing now the behaviour of each controller type, if we define a settling time threshold of 0.5% of the reference value then the PI controller has the shortest settling time of 0.27 s followed by the PID controller with 0.31 s. Due to its steady state error, the P controller never reaches within 0.5% of the reference value. The PID controller exhibits a 2.0% overshoot which is larger than the PI controller with 1.0%. Based on these characteristics it appears that both controllers are suitably tuned for the system despite the discrepancy in analytical model behaviour, with the PI controller exhibiting slightly better performance than the PID controller. Ideally the controllers would not reach saturation for a step of this size, but the effects should be minimal.

5 Assessment of Small-Signal Stability

Generally, it was observed that the integrated model, consisting of a synchronous generator connected to a grid forming inverter with a shared passive load, was a robust system. Under the range of testing conditions in Sections 5.1 and 5.2, no instability was observed when the generator and inverter output a nominal $S = 1$ pu. In order reduce system robustness, the power output was increased to $S = 1.3$ pu by decreasing the passive load by $1/1.3 \approx 77\%$. Under these conditions, some instances of instability were observed, but generally, for most tests the system remained stable under a small-signal perturbation. This would suggest that the interactions between synchronous generator and grid forming controls are generally stable and will not inherently result in instability under normal conditions.

The test procedure for the following sections (unless otherwise stated) are as follows:

1. Start the system as per Section 3.2
2. Allow system to stabilise with both the inverter and generator producing $S = 1.3$ pu.
3. At $t = 55$, connect a parallel load which reduces the effective impedance to 91% of pre-disturbance conditions, increasing the power draw by $S = 1/0.91 = 1.1$ pu.
4. At $t = 75$, disconnect the parallel load to restore the effective impedance to pre-disturbance conditions.

The rotor-angle stability will be the primary criteria of robustness for each test. As such, a configuration will be deemed 'stable' if the initial disturbance produces oscillations which decay overtime, that is to say, the configuration has sufficient damping torque. A configuration will be deemed 'unstable' if oscillations from the disturbance continue to grow until the rotor angle exceeds the critical threshold.

The stability of a test configuration, be that a particular excitation control variant or change in machine parameter, will be assessed by incrementally reducing the transmission line length until instability occurs. Instability is expected at shorter line lengths, because the effective impedance between the two voltage sources reduces, which leads to more sensitivity in control interactions and potentially higher current draw during oscillations. The line length at which instability is reached is the performance criteria for the robustness of the configuration.

5.1 Impact of Control Variants

All control variants and line lengths were found to be stable for the nominal inverter low-pass cut off frequency of $f_{\text{LPF}} = 5$ Hz. f_{LPF} was reduced to 2 Hz, at which, instability was observed in both the PI and PID control variants. The critical line lengths for each

controller type, that is, the line lengths at which instability first occured, are presented in Table 4. Considering these results, it is reasonable to state that the excitation system with a PID controller was the least robust, followed by the PI controller, and then the P controller for which no instability was observed.

Table 4: The critical line length for each controller type. $S = 1.3$ pu, $f_{\text{LPF}} = 2$ Hz.

Controller Type	Critical Line Length
P	-
PI	47 km
PID	56 km

It was observed that the system was least robust between 30 and 40 km. After which, shortening the line length had the effect of increasing the damping torque and improving system robustness. This is not a result which was expected, and the underlying causal mechanism is not clear. Excitation saturation was investigated as a potential cause; increasingly larger initial oscillations are observed at the output of the exciter as the line length shortens, resulting in longer periods at which the excitation is saturated at the lower bound of $E_{\text{fd}} = 0$, which could potentially introduce extra damping. However, for P controlled systems, the excitation output never reaches saturation, even for short line lengths. Despite this, the robustness of the system still improves below 30 km, and so this phenomenon cannot be due to excitation saturation. This behaviour had not been observed in previous iterations of the simulation model during development, thus there is the possibility that this is caused by an unintended change in the simulation model. Future work should consider whether this behaviour is a fundamental observation of the system or a result of the simulation model, and more investigation could be performed to identify the root cause.

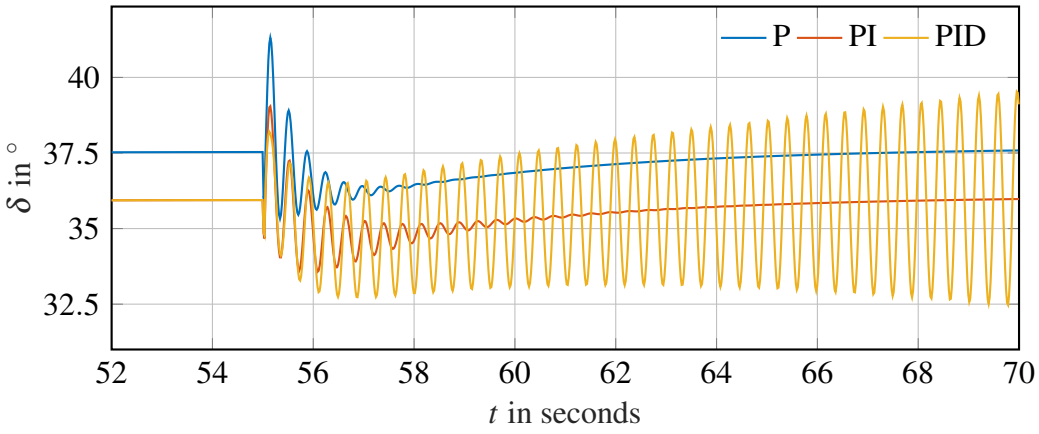

Figure 29: Step response of P, PI, and PID excitation controllers for 40 km line length, $f_{\text{LPF}} = 3$ Hz at $S = 1.3$ pu

Figure 29 shows rotor angle δ for each excitation control variant using the same system configuration, where the PID controlled excitation system is unstable and the PI and P controlled

systems are stable. It can be seen that, when the load step occurs, each control variant experiences a disturbance of equal magnitude which results in ∼2.6 Hz oscillations. But while the PI and PID controllers sufficiently damp this disturbance, the PID controller lacks sufficient damping torque and the oscillation grows. Between the PI and P controllers, the PI has less damping than the P, with visible oscillations persisting until $t = 62$ s.

Figure 30 shows system behaviour for the same configuration as Figure 29. It is noted that, unlike the infinite bus model, the excitation output never reaches the upper saturation limit. This could indicate that additional impedance in the network damps the voltage response for the disturbance and thus reduces the response from the excitation control. The PID excitation system does reach the minimum saturation bounds 0.08 s after the disturbance, and stays saturated for 0.04 s. It was observed that as the line length shortens, the saturation duration increases, even with the increasing robustness, but never exceeds 0.1 s.

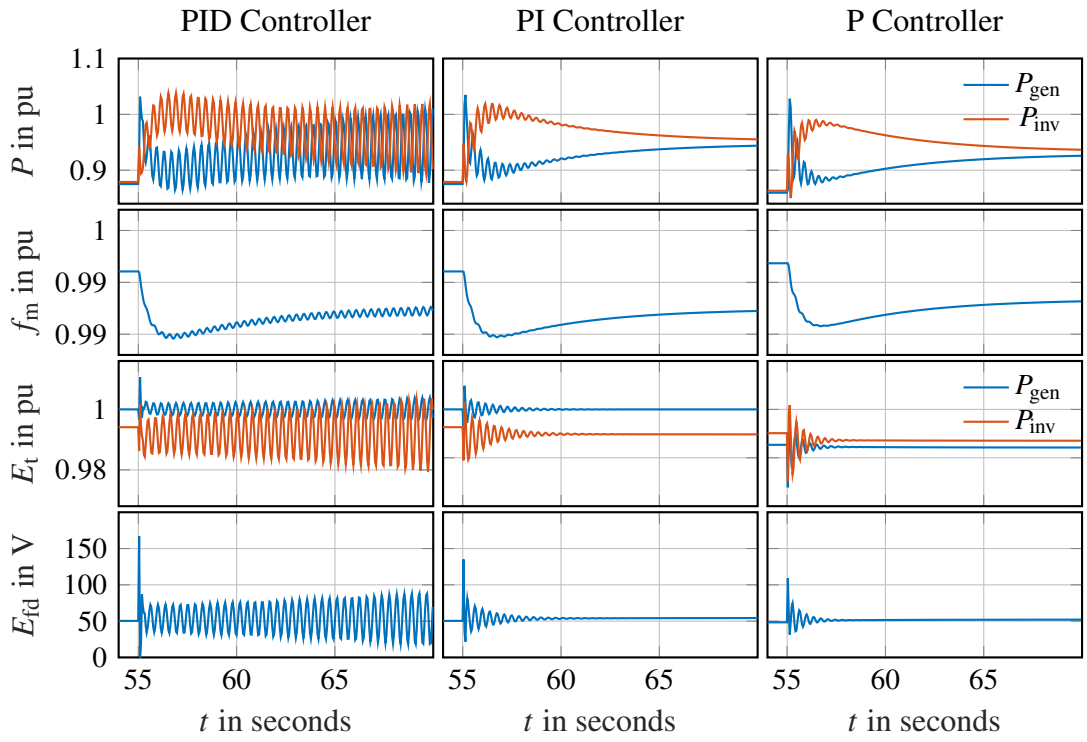

Figure 30: Behaviour of PID and PI controlled excitation systems for a 40 km line length with $f_{LPF} = 3$ Hz at $S = 1.3$ pu

It can also be seen that the P controlled excitation system never reaches nominal terminal voltage due to the steady state error in the controller. As a result, the power output is less than the other controllers, which may improve system robustness. However, any improvements in robustness are outweighed by an insufficient terminal voltage which is undesirable in actual operating assets.

Finally, for all tests performed, the output of the inverter droop paths were observed in order

to determine if the gain outputs reached saturation, as this may introduce other destabilising effects. In all tests neither inverter droop gain reached saturation. The effect of the droop paths are discussed further in Section 5.5.

5.2 Impact of Frequency Droop Cutoff Frequency

The simulation was repeated for a range of f_{LPF} values to test its impact on small-signal stability for the integrated system. f_{LPF} is inversely proportional to the inertia of the inverter, and so decreasing its value should result in better disturbance rejection and more robustness. However, it has been observed in literature that decreasing f_{LPF} reduces the phase margin of the power droop control, which can itself hinder small-signal stability (Wu et al., 2016).

The results show that, as f_{LPF} is reduced, the system robustness is reduced, with values of $f_{\mathrm{LPF}} = 2$ Hz producing instability in the PI and PID controlled excitation systems, and $f_{\mathrm{LPF}} = 3$ Hz producing instability in the PID controlled excitation systems at $S = 1.3$ pu. Beyond these cut-off frequency values, no instability was observed for any control type. This shows that the impact of phase margin reduction has a much more significant effect on small-signal stability than the reduction of inertia. For the PID controller, the range of cut-off frequency was extended up to a maximum of $f_{\mathrm{LPF}} = 100$ Hz to see whether the lack of inertia would reduce robustness after a certain threshold. No such reduction was observed, which agrees with findings stated in (Markovic et al., 2021).

Figure 31 shows the generator rotor angle for a range of cut-off frequencies with a PI controller. Tables 5, 6, and 7 show the stability of each line length, f_{LPF} and controller variant combination. It is noted in these tables that some simulations either became unstable before the step response, labelled in purple, or out-right failed, labelled in orange. In the former, the simulation would become unstable after the power was ramped to $S = 1.3$ pu but before the load step at $t = 55$ s. This could be viewed as a form of small-signal instability, showing that the system configuration is not stable, however these results were differentiated as they cannot be directly compared with the unstable results from the load step, as the magnitude of the disturbance is different. For the latter, simulations failed due to numerical issues in the Simulink solver and did not provide any meaningful results. This was due to excessive zero-crossings, requiring the solver to reduce the simulation step size to such a small step that the simulation would not progress within any reasonable time frame. In an attempt to resolve this, the minimum step size was increased, however in testing against successful results, the broad stability behaviour of the system was seen to change and so the tests were deemed invalid.

Table 5: System stability with a PID controlled excitation system for a range of line lengths and f_{LPF}

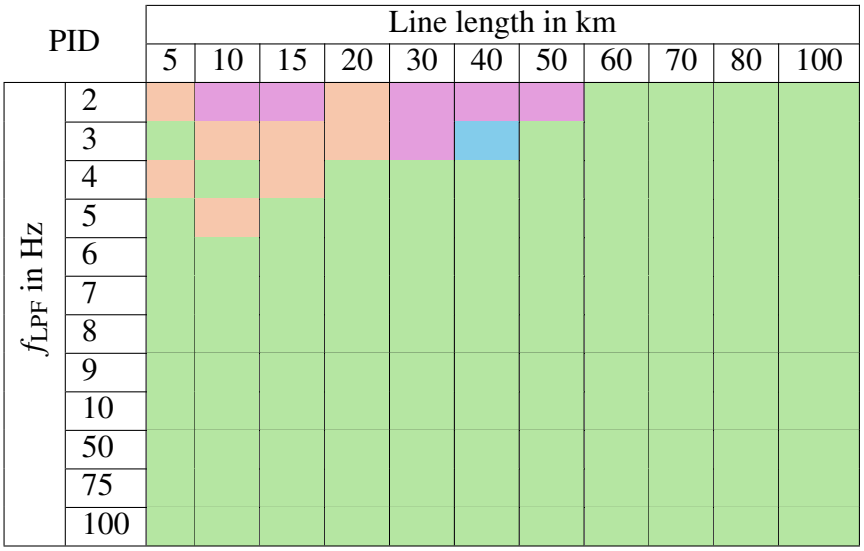

Table 6: System stability with a PI controlled excitation system for a range of line lengths and f_{LPF}

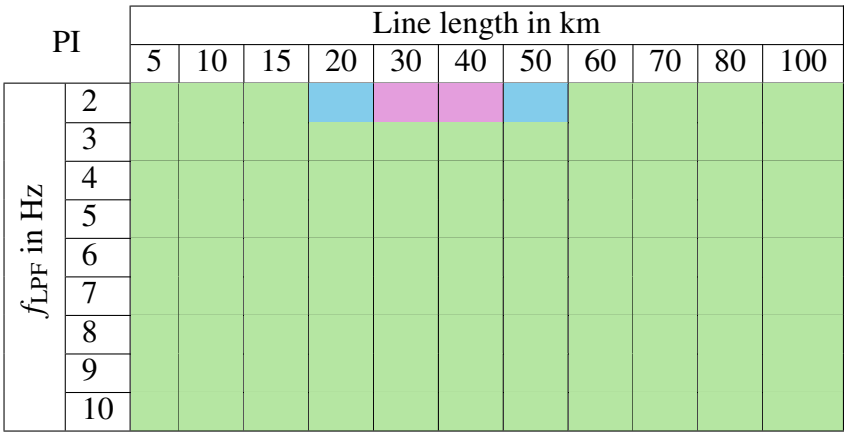

Table 7: System stability with a P controlled excitation system for a range of line lengths and f_{LPF}

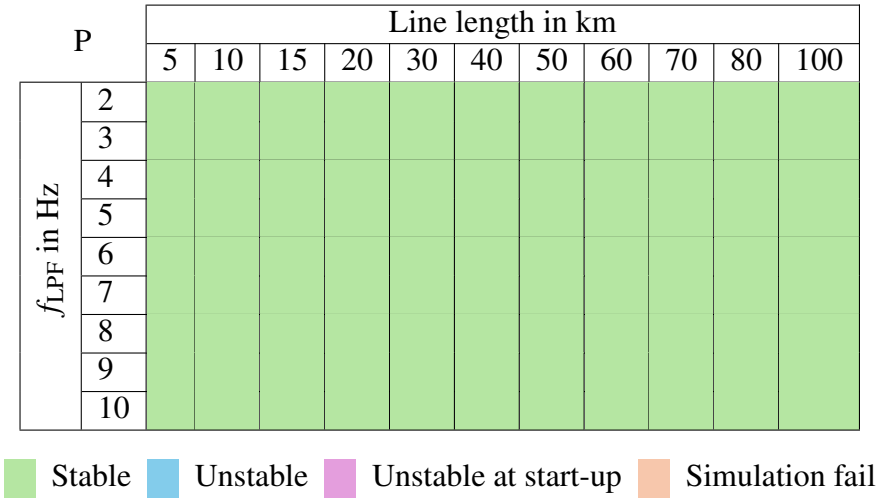

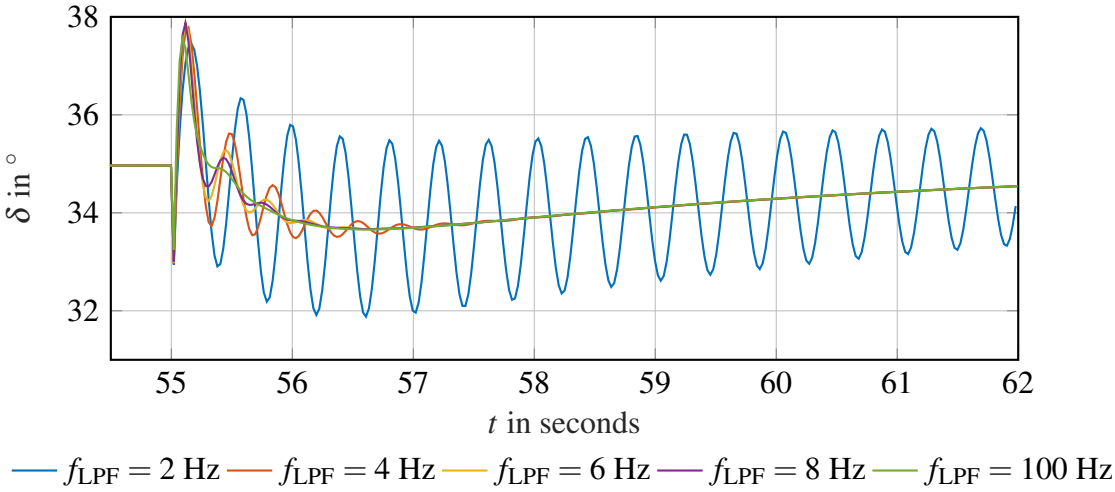

Figure 31: A sweep of f_{LPF} for a PI controller with 40km line length at $S = 1$ pu

5.3 Impact of PSS

In previous instances of instability, the frequency of the oscillations were observed to be between 2 and 3 Hz. This is the damping target frequency for a PSS tuned for single machine interactions (Kundur, 2009), and so it is expected the PSS will effectively reduce system oscillations. The results from simulations performed with a PSS showed this to be true. For all unstable conditions observed in Section 5.2, the PSS effectively damped oscillations and maintained stability. Figure 32 shows a PID controlled excitation system in an unstable configuration without a PSS, and then with a PSS. It can be seen that the PSS is extremely effective at damping oscillations.

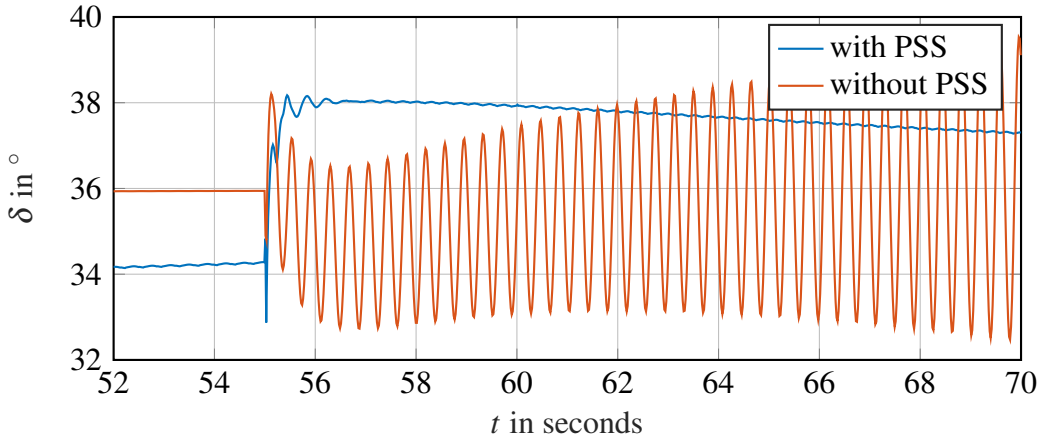

Figure 32: A PID controlled excitation system with a 40 km line length at $S = 1.3$ pu with and without a PSS

It has been noted in literature that the tuning of the PSS affects the effectiveness of oscillation damping between synchronous generators and grid forming inverters (Crivellaro et al., 2020). PSS tuning is influenced by the requirements of the application; in network connected power

systems a PSS might be tuned to act on broad inter-area network oscillations which have can have frequencies as low as 0.2 Hz. Such PSSs might not be as effective at damping the oscillations observed within this study. The PSS parameters used are from (Zhang et al., 2023), which have been tuned for small scale network interactions. Future work could use the model to assess the impact of PSS tuning and to evaluate the effectiveness of models tuned for different system goals.

5.4 Impact of Frequency Droop Slopes

The impact of the frequency droop settings in the generator, R and inverter, m_{P}, were tested with simulations at $S = 1$ pu, $f_{\mathrm{LPF}} = 3$ Hz with a line length of 40 km for a combination of 1% and 10% droop settings. The droops gains are expressed as percentage values based on nominal frequency and power values. To state the inverter specifically, the nominal gain m_{P}, may be expressed as a percentage value $m_{\mathrm{P}\%}$ by

$$m_{\mathrm{P}} = \frac{2.5\ \mathrm{Hz} \cdot 2\pi}{P_0} \quad \Rightarrow \quad m_{\mathrm{P}\%} = \frac{(2.5\ \mathrm{Hz} \cdot 2\pi)/(50\ \mathrm{Hz} \cdot 2\pi)}{P_0/P_0} \cdot 100\% = 5\%$$

Figure 33 shows the generator rotor angle for different combinations of the tested droop settings when subject to a step response. For the generator or inverter, as the droop percentage increases, more of the load is supplied proportionally. It is clear that increasing the inverter droop gain has the effect of increasing the frequency and amplitude of oscillations, and reducing system damping. Increasing the generator droop gain has the effect of changing the shape of the disturbance. This result aligns with expectation, as the time constants associated with the inverter frequency control are orders of magnitude smaller than those associated with the generator frequency control. As a result, when the inverter supplies more load proportionally, it contributes more to the disturbance response, and hence oscillations occur according to the inverter's time constants. The generator has a turbine time constant of $T_{\mathrm{G}} = 10$ s, and as its contribution to the load increases, it introduces oscillations on this time scale, hence appearing to change the shape of the response.

5.5 Identification of the Role of Inverter Droop Paths in Instability

It has been seen that reducing f_{LPF} reduces system robustness by lowing the phase margin of the power droop control. Additionally, increasing m_{P} exacerbated instability. These two results would seem to suggest that the instability observed between the grid forming inverter and synchronous generator involves interactions with the droop control of the inverter. This can be tested by using an unstable system configuration, and disabling the P-ω and Q-V droop paths respectively to observe the effect on system stability.

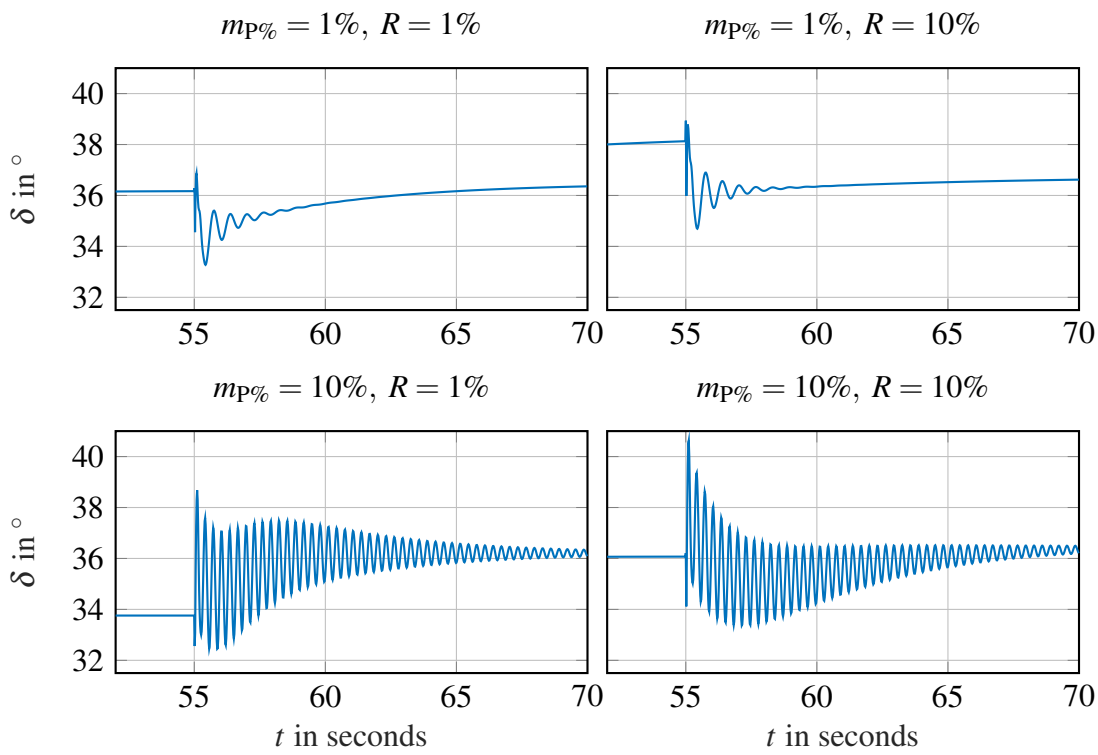

Figure 33: Effect of droop slope setting on the rotor angle stability for a 40 km line length with $f_{\text{LPF}} = 3$ Hz at $S = 1$ pu

Figure 34 shows the power responses of the inverter and generator with each inverter droop path disabled for a PID excitation system with $S = 1.3$ pu, $f_{\text{LPF}} = 3$ Hz and a 40 km line length. It is observed that with each droop path disabled, two distinct oscillation patterns emerge. With P-ω droop disabled a $\sim$1.2 Hz oscillation occurs within the Q-V droop path, which can also be seen in Figure 35. With the Q-V droop disabled, a much lower amplitude $\sim$2.5 Hz oscillation can be observed in the P-ω droop path. Interestingly, both cases result in a stable system, despite the configuration producing instability when both droop paths are enabled.

This result suggests that distinct oscillation modes exist within the respective inverter droop paths and that both contribute to instances of small-signal instability. The frequency of oscillations observed with both paths enabled were $\sim$2.5 Hz, which more closely matched the mode within the P-ω path. However, the amplitude of the oscillation mode within the Q-V path was relatively larger which would suggest that its contribution is higher, although, this may be a result of the disparity in supply power at the time of disturbance as seen with the droop magnitude tests. Future work could explore the inverter model in greater detail to determine what control actions contribute to the instability observed and to what degree.

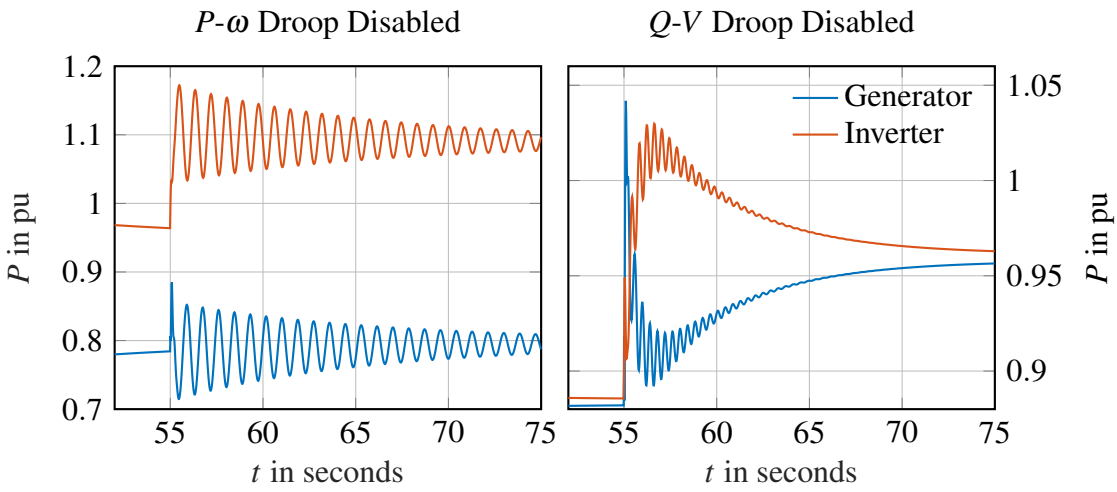

Figure 34: Power response of system with inverter droop paths disabled at $S = 1.3$ pu with $f_{\text{LPF}} = 3$ Hz and a 40 km line length

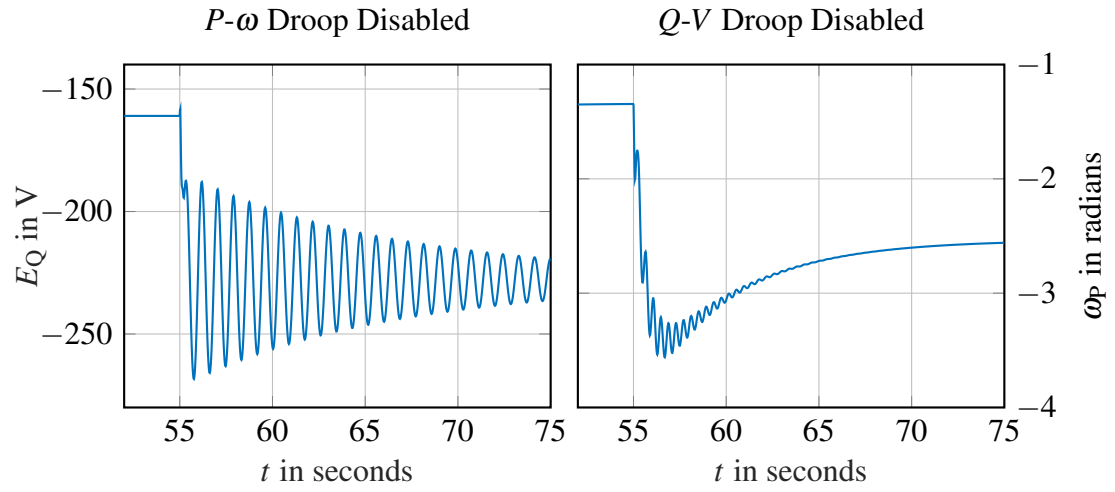

Figure 35: Output of inverter droop gains at $S = 1.3$ pu with $f_{\text{LPF}} = 3$ Hz and a 40 km line length

6 Conclusion and Future Prospects

This thesis examines the effect of controller variants in excitation systems and their impact on small-signal stability when interacting with grid forming inverters. The effects are examined using EMT simulations. For the PI and PID controller variants, the gain values were tuned using analytical techniques based on a derived analytical model of the synchronous generator. The results show that there is a possibility for destabilising behaviour to be introduced by PI and PID controllers, as compared using solely a P controller. This indicates that current literature which examines the stability of synchronous generator and grid forming interactions, may be over-estimating system robustness by using simplified excitation control schemes. However, it was demonstrated that a PSS can effectively dampen oscillations and return the system to stability.

An analytical model for the synchronous generator in an infinite bus was derived, resulting in a 7^{th}-order transfer function representing the dynamics between a terminal voltage set-point and the measured terminal voltage as observed by the excitation system. This transfer function was used to tune a PI and PID controller using the symmetrical optimum and internal model controller techniques respectively. The resultant controllers were verified within an EMT simulation and their behaviour was shown to be reasonable. However, the derived analytical model showed significant deviation in behaviour when compared to the simulated model, particularly concerning the zero frequency gain and resulting steady state error when using a P type controller. This implies that an issue may be present in the analytical model derivation, and a potential solution of including a Thévenin equivalent network impedance within the infinite bus model was suggested. The discrepancy in behaviour could impact the validity of the PI and PID tuning, and if these controllers were improperly tuned, then the results of the experiments could be attributed to their tuning, rather than due to effects between the generator and grid forming inverter. However, since the PI and PID controllers performed adequately in both infinite bus and integrated simulation models when compared against the given P type tuning, it is unlikely that the controllers are completely mistuned and the results observed should still be pertinent to the interactions between grid forming inverters and synchronous generators.

Generally the system was found to be robust, and under nominal operating conditions, small-signal instability could not be induced. By increasing operational load and iteratively reducing the transmission line length, instability was observed first in the PID type controller, making it the least robust, then in the PI controller. The impact of the inverter droop cut-off frequency was tested and found that lowing the cut-off frequency reduced system robustness despite the theoretical inertial increase. PSSs were added to unstable system configurations

and found to effectively eliminate all instability. Finally, the droop settings of the generator and inverter were investigated, with results suggesting that the inverter droop control, particularly the $P-\omega$ droop path plays a critical role in instability interactions.

Future work can build upon the derived simulation models to test alternative settings and scenarios, and observe their impact on system stability. Some interesting alternatives would be to evaluate the impact of PSS tuning on the stability of the system, particularly with PSSs tuned to other system goals, such as low frequency inter-area oscillations. Furthermore, the model could be extended to cover other grid scenarios, such as including grid following inverters, more complicated grid bus structures, and different penetration levels of each technology. Future work may also extend the model of the excitation system to allow for negative excitation voltage which may reveal other stability interactions, or to include other subsystems which are included in real operating synchronous generators.

References

Boldea, I. (2006). *Synchronous Generators*. The Electric Generators Handbook 1. Boca Raton, Fla.: CRC, Taylor & Francis. ISBN: 978-0-8493-5725-1.

Chapman, S. J. (2005). *Electric Machinery Fundamentals*. 4th ed. New York, NY: McGraw-Hill Higher Education. 746 pp. ISBN: 978-0-07-246523-5.

Crivellaro, A., Tayyebi, A., Gavriluta, C., Groß, D., Anta, A., Kupzog, F. & Dörfler, F. (Aug. 2020). Beyond Low-Inertia Systems: Massive Integration of Grid-Forming Power Converters in Transmission Grids. In: *2020 IEEE Power & Energy Society General Meeting (PESGM)*. 2020 IEEE Power & Energy Society General Meeting (PESGM), pp. 1–5. DOI: 10.1109/PESGM41954.2020.9282031. URL: https://ieeexplore.ieee.org/document/9282031/ (visited on 04/24/2025).

D'Arco, S. & Suul, J. A. (Jan. 2014). Equivalence of Virtual Synchronous Machines and Frequency-Droops for Converter-Based MicroGrids. *IEEE Transactions on Smart Grid* 5(1), pp. 394–395. ISSN: 1949-3053, 1949-3061. DOI: 10.1109/TSG.2013.2288000. URL: http://ieeexplore.ieee.org/document/6683080/ (visited on 09/30/2025).

"Damper Windings and Damping" (2010). In: Kimbark, E. W. *Power System Stability*. IEEE. ISBN: 978-0-470-54561-4. DOI: 10.1109/9780470545614.ch14. URL: https://ieeexplore.ieee.org/document/5488877 (visited on 10/07/2025).

"Definition and Classification of Power System Stability IEEE/CIGRE Joint Task Force on Stability Terms and Definitions" (Aug. 2004). *IEEE Transactions on Power Systems* 19(3), pp. 1387–1401. ISSN: 0885-8950. DOI: 10.1109/TPWRS.2004.825981. URL: http://ieeexplore.ieee.org/document/1318675/ (visited on 10/05/2025).

Demello, F. & Concordia, C. (Apr. 1969). Concepts of Synchronous Machine Stability as Affected by Excitation Control. *IEEE Transactions on Power Apparatus and Systems* PAS-88(4), pp. 316–329. ISSN: 0018-9510. DOI: 10.1109/TPAS.1969.292452. URL: http://ieeexplore.ieee.org/document/4073838/ (visited on 10/04/2025).

Eurostat (Sept. 2025). *Maximum Electrical Capacity, EU, 2010 - 2023*. nrg_inf_epc. URL: https://ec.europa.eu/eurostat/statistics-explained/index.php?title=Electricity_and_heat_statistics (visited on 10/24/2025).

Garcia, C. E. & Morari, M. (Apr. 1982). Internal Model Control. A Unifying Review and Some New Results. *Industrial & Engineering Chemistry Process Design and Development* 21(2), pp. 308–323. ISSN: 0196-4305, 1541-5716. DOI: 10.1021/i200017a016. (Visited on 09/24/2025).

Gibbard, M., Pourbeik, P. & Vowles, D. (2015). *Small-Signal Stability, Control and Dynamic Performance of Power Systems*.

IEEE (Aug. 2016). *IEEE Recommended Practice for Excitation System Models for Power System Stability Studies*. DOI: 10.1109/IEEESTD.2016.7553421. URL: https://ieeexplore.ieee.org/document/7553421/ (visited on 06/12/2025).

Kiam Heong Ang, Chong, G. & Yun Li (July 2005). PID Control System Analysis, Design, and Technology. *IEEE Transactions on Control Systems Technology* 13(4), pp. 559–576. ISSN: 1063-6536. DOI: 10.1109/TCST.2005.847331. URL: http://ieeexplore.ieee.org/document/1453566/ (visited on 10/25/2025).

Kundur, P. (2009). *Power System Stability and Control*. McGraw-Hill.

Landau, I. & Voda, A. (July 1992). The "Symmetrische Optimum" and the Auto-Calibration of PID Controllers. *IFAC Proceedings Volumes* 25(14), pp. 407–412. ISSN: 14746670. DOI: 10.1016/S1474-6670(17)50768-5. (Visited on 09/24/2025).

Li, J. (2019). *Design and Application of Modern Synchronous Generator Excitation Systems*. 1st ed.

Markovic, U., Stanojev, O., Aristidou, P., Vrettos, E., Callaway, D. & Hug, G. (Sept. 2021). Understanding Small-Signal Stability of Low-Inertia Systems. *IEEE Transactions on Power Systems* 36(5), pp. 3997–4017. ISSN: 1558-0679. DOI: 10.1109/TPWRS.2021.3061434. URL: https://ieeexplore.ieee.org/document/9361257/?arnumber=9361257 (visited on 03/14/2025).

O'Dwyer, A. (2009). *Handbook of PI and PID Controller Tuning Rules*. 3rd ed. London: Imperial College Press. 1 p. ISBN: 978-1-84816-242-6 978-1-84816-243-3.

Oeding, D. & Oswald, B. R. (2016). *Elektrische Kraftwerke und Netze*. Berlin, Heidelberg: Springer Berlin Heidelberg. ISBN: 978-3-662-52702-3 978-3-662-52703-0. DOI: 10.1007/978-3-662-52703-0. URL: http://link.springer.com/10.1007/978-3-662-52703-0 (visited on 09/02/2025).

Ogata, K. (2022). *Modern Control Engineering*. 5th ed. Prentice Hall. ISBN: 978-0-13-615673-4.

Pyrhönen, J., Jokinen, T. & Hrabovcová, V. (2014). Windings of Electrical Machines. In: *Design of Rotating Electrical Machines*. Second edition. Chichester: Wiley. ISBN: 978-1-118-70165-2 978-1-118-70162-1 978-1-118-58157-5.

Rathnayake, D. B., Akrami, M., Phurailatpam, C., Me, S. P., Hadavi, S., Jayasinghe, G., Zabihi, S. & Bahrani, B. (2021). Grid Forming Inverter Modeling, Control, and Applications. *IEEE Access* 9, pp. 114781–114807. ISSN: 2169-3536. DOI: 10.1109/ACCESS.2021.3104617. URL: https://ieeexplore.ieee.org/document/9513281/?arnumber=9513281 (visited on 03/14/2025).

Sauer, P. W. & Pai, M. A. (2007). *Power System Dynamics and Stability*.

Schröder, D. & Böcker, J., eds. (2021). *Elektrische Antriebe Regelung von Antriebssystemen*. Berlin, Heidelberg: Springer Berlin Heidelberg. ISBN: 978-3-662-62699-3 978-3-662-

62700-6. DOI: 10.1007/978-3-662-62700-6. URL: http://link.springer.com/10.1007/978-3-662-62700-6 (visited on 09/09/2025).

Strunk, R. & Mertens, A. (Sept. 2023). Impedance-Based Stability Analysis of Droop-Controlled AC Microgrids with the Generalized Nyquist Criterion. In: *2023 25th European Conference on Power Electronics and Applications (EPE'23 ECCE Europe)*, pp. 1–10. DOI: 10.23919/EPE23ECCEEurope58414.2023.10264611. (Visited on 10/21/2025).

Tayyebi, A., Groß, D., Anta, A., Kupzog, F. & Dörfler, F. (June 2020). Frequency Stability of Synchronous Machines and Grid-Forming Power Converters. *IEEE Journal of Emerging and Selected Topics in Power Electronics* 8(2), pp. 1004–1018. ISSN: 2168-6785. DOI: 10.1109/JESTPE.2020.2966524. URL: https://ieeexplore.ieee.org/document/8959148/ (visited on 04/24/2025).

Tielens, P. & Van Hertem, D. (Mar. 2016). The Relevance of Inertia in Power Systems. *Renewable and Sustainable Energy Reviews* 55, pp. 999–1009. ISSN: 13640321. DOI: 10.1016/j.rser.2015.11.016. URL: https://linkinghub.elsevier.com/retrieve/pii/S136403211501268X (visited on 10/24/2025).

Wu, H., Ruan, X., Yang, D., Chen, X., Zhao, W., Lv, Z. & Zhong, Q.-C. (July 2016). Small-Signal Modeling and Parameters Design for Virtual Synchronous Generators. *IEEE Transactions on Industrial Electronics* 63(7), pp. 4292–4303. ISSN: 1557-9948. DOI: 10.1109/TIE.2016.2543181. URL: https://ieeexplore.ieee.org/document/7434595/ (visited on 10/23/2025).

Zhang, Y., Wiese, N., Liu, Z. & Braun, M. (Oct. 2023). On the Control Interaction of Synchronous Machine and Inverter-Based Resources during System-Split Situations. *International Journal of Electrical Power & Energy Systems* 152, p. 109227. ISSN: 01420615. DOI: 10.1016/j.ijepes.2023.109227. URL: https://linkinghub.elsevier.com/retrieve/pii/S0142061523002843 (visited on 04/29/2025).

Appendix 1 Analytical Model Coefficients

1.1 Calculation Coefficients

$$m_1 = \frac{E_G}{D}(X_{Tq}\sin\delta_0 - R_T\cos\delta_0) \quad m_2 = \frac{X_{Tq}L'_{ad}}{DL_{1d}}$$
$$m_3 = \frac{X_{Tq}L'_{ad}}{DL_{1d}} \quad m_4 = -\frac{R_TL'_{aq}}{DL_{1q}} \quad m_5 = -\frac{R_TL'_{aq}}{DL_{2q}}$$
$$n_1 = \frac{E_G}{D}(R_T\sin\delta_0 + X_{Tq}\cos\delta_0) \quad n_2 = \frac{R_TL'_{ad}}{DL_{1d}}$$
$$n_3 = \frac{R_TL'_{ad}}{DL_{1d}} \quad n_4 = \frac{X_{Tq}L'_{aq}}{DL_{1q}} \quad n_5 = \frac{X_{Tq}L'_{aq}}{DL_{2q}}$$

$$K_1 = n_1\left(\Psi_{ad0} + L'_{aq}i_{d0}\right) - m_1\left(\Psi_{aq0} + L'_{ad}i_{q0}\right) + \frac{L'_{ad}}{L_{fd}}i_{q0}$$
$$K_2 = n_2\left(\Psi_{ad0} + L'_{aq}i_{d0}\right) - m_2\left(\Psi_{aq0} + L'_{ad}i_{q0}\right) + \frac{L'_{ad}}{L_{fd}}i_{q0}$$
$$K_{21} = n_3\left(\Psi_{ad0} + L'_{aq}i_{d0}\right) - m_3\left(\Psi_{aq0} + L'_{ad}i_{q0}\right) - \frac{L'_{ad}}{L_{1d}}i_{q0}$$
$$K_{22} = n_4\left(\Psi_{ad0} + L'_{aq}i_{d0}\right) - m_4\left(\Psi_{aq0} + L'_{ad}i_{q0}\right) - \frac{L'_{aq}}{L_{1q}}i_{d0}$$
$$K_{23} = n_5\left(\Psi_{ad0} + L'_{aq}i_{d0}\right) - m_5\left(\Psi_{aq0} + L'_{ad}i_{q0}\right) - \frac{L'_{aq}}{L_{2q}}i_{d0}$$

$$K_5 = \frac{L'_{ad}m_5 + L_l n_5 - R_s m_5}{E_{t0}}e_{d0} + \left(\frac{L_l m_5 + R_s n_5 + L'_{aq}\left(n_5 - \frac{1}{L_{2q}}\right)}{E_{t0}}\right)e_{q0}$$
$$K_6 = \frac{L'_{ad}m_4 + L_l n_4 - R_s m_4}{E_{t0}}e_{d0} + \left(\frac{L_l m_4 + R_s n_4 + L'_{aq}\left(n_4 - \frac{1}{L_{1q}}\right)}{E_{t0}}\right)e_{q0}$$
$$K_{61} = \frac{L_l n_3 - R_s m_3 + L'_{ad}\left(m_3 - \frac{1}{L_{1d}}\right)}{E_{t0}}e_{d0} - \frac{L_l m_3 + L'_{aq}n_3 - R_s n_3}{E_{t0}}e_{q0}$$
$$K_{62} = \frac{L_l n_2 - R_s m_2 + L'_{ad}\left(m_2 - \frac{1}{L_{fd}}\right)}{E_{t0}}e_{d0} - \frac{L_l m_2 + L'_{aq}n_2 - R_s n_2}{E_{t0}}e_{q0}$$
$$K_{63} = \frac{L'_{ad}m_1 + L_l n_1 - R_s m_1}{E_{t0}}e_{d0} - \frac{L_l m_1 + L'_{aq}n_1 - R_s n_1}{E_{t0}}e_{q0}$$

1.2 State space formula

1.2.1 Plant Matrix

$$a_{11} = -\frac{K_D}{2H} \quad a_{12} = -\frac{K_1}{2H} \quad a_{13} = -\frac{K_2}{2H} \quad a_{14} = -\frac{K_{21}}{2H} \quad a_{15} = -\frac{K_{22}}{2H} \quad a_{16} = -\frac{K_{23}}{2H}$$

$$a_{21} = \omega_0 \quad a_{32} = -\frac{\omega_0 R_{fd}}{L_{fd}} m_1 L'_{ad} \quad a_{33} = -\frac{\omega_0 R_{fd}}{L_{fd}} \left(1 - \frac{L'_{ad}}{L_{fd}} + m_2 L'_{ad}\right)$$

$$a_{34} = -\frac{\omega_0 R_{fd}}{L_{fd}} \left(m_3 L'_{ad} - \frac{L'_{ad}}{L_{fd}}\right) \quad a_{35} = -\frac{\omega_0 R_{fd}}{L_{fd}} m_4 L'_{ad} \quad a_{36} = -\frac{\omega_0 R_{fd}}{L_{fd}} m_5 L'_{ad}$$

$$a_{43} = -\frac{\omega_0 R_{1d}}{L_{1d}} \left(m_2 L'_{ad} - \frac{L'_{ad} L'_{ad}}{L_{fd}}\right) \quad a_{44} = -\frac{\omega_0 R_{1d}}{L_{1d}} \left(1 - \frac{L'_{ad}}{L_{fd}} + m_3 L'_{ad}\right)$$

$$a_{45} = -\frac{\omega_0 R_{1d}}{L_{1d}} m_4 L'_{ad} \quad a_{46} = -\frac{\omega_0 R_{1d}}{L_{1d}} m_5 L'_{ad} \quad a_{52} = -\frac{\omega_0 R_{1q}}{L_{1q}} n_1 L'_{aq}$$

$$a_{53} = -\frac{\omega_0 R_{1q}}{L_{1q}} n_2 L'_{aq} \quad a_{54} = -\frac{\omega_0 R_{1q}}{L_{1q}} n_3 L'_{aq} \quad a_{55} = -\frac{\omega_0 R_{1q}}{L_{1q}} \left(1 - \frac{L'_{aq}}{L_{1q}} + n_4 L'_{aq}\right)$$

$$a_{56} = -\frac{\omega_0 R_{1q}}{L_{1q}} \left(n_5 L'_{aq} - \frac{L'_{aq} L'_{aq}}{L_{2q}}\right) \quad a_{62} = -\frac{\omega_0 R_{2q}}{L_{2q}} n_1 L'_{aq} \quad a_{63} = -\frac{\omega_0 R_{2q}}{L_{2q}} n_2 L'_{aq}$$

$$a_{64} = -\frac{\omega_0 R_{2q}}{L_{2q}} n_3 L'_{aq} \quad a_{65} = -\frac{\omega_0 R_{2q}}{L_{2q}} \left(n_4 L'_{aq} - \frac{L'_{aq} L'_{aq}}{L_{1q}}\right) \quad a_{66} = -\frac{\omega_0 R_{2q}}{L_{2q}} \left(1 - \frac{L'_{aq}}{L_{2q}} + n_5 L'_{aq}\right)$$

1.2.2 Input Matrix

$$b_{11} = \frac{1}{2H} \quad b_{32} = \frac{\omega_0 R_{fd}}{L_{ad}}$$